TECHNISCHE
UNIVERSITÄT
WIEN
Vienna University of Technology

Diplomarbeit

Probing solid-state electron spin-phonon interaction at the quantum limit

ausgeführt am Atominstitut der Technischen Universität Wien unter der Anleitung von

Univ. Prof. Dr. Hannes-Jörg Schmiedmayer

Univ. Ass. Dr. Johannes Majer

Projektass. Dipl.-Ing. Thomas Astner

Projektass. Dipl.-Ing. Andreas Angerer

eingereicht an der
Technischen Universität Wien
Fakultät für Physik

von

Sebastian Wald

Matrikelnummer: 1026377

Hanuschstraße 30, 4400 Steyr

Wien, am 24. Oktober 2017

Abstract

Longitudinal relaxation, which is the interaction of quantum systems with their environment, gives a limitation of the lifetime of quantum states. Hence, the longitudinal relaxation time T_1 is a characteristic measure for quantum systems and their maximally attainable coherence time $(T_2 \leq 2\,T_1)$.

A promising physical system for the realization of quantum technologies like quantum communication, information processing and metrology is the negatively charged nitrogen-vacancy color center (NV^-) in diamond. The longitudinal relaxation of the NV^- electron spin ensemble is driven by spin-phonon interaction and has been studied in a 'high' temperature regime $(4\,\mathrm{K})$ only.

In this thesis, a cavity quantum electrodynamics measurement scheme for spin-phonon relaxation of NV^- ensembles in a temperature regime of 25-250 mK is presented. We introduce a 3D microwave resonator design, which enables homogeneous single spin coupling. Furthermore, we are able to measure the spin polarization indirectly in the dispersive regime to observe longitudinal relaxation.

A maximum $T_1 \approx 8\,\mathrm{h}$ indicates weak spin-phonon coupling. With temperature scans, we determine the direct spin-phonon process as fundamental origin of this relaxation and show that in a temperature regime of $k_B T < \hbar \omega_s$, T_1 is only limited by the spontaneous emission of spin excitations into the phononic vacuum modes.

Furthermore, we compare four different diamond samples to investigate the influence of lattice damage on the longitudinal relaxation. We are able to show that the measured data of two samples almost show the calculated relaxation behaviour of a single NV^- in a perfect crystal.

Zusammenfassung

Longitudinale Relaxation, der Zerfall eines Quantenzustandes durch die Wechselwirkung mit seiner Umgebung limitiert die Lebensdauer des Zustandes. Charakterisiert wird dieser Zerfall durch die longitudinale Relaxationszeit T_1. Diese Messgröße ist charakteristisch für verschiedene Quantensysteme und beschreibt auch deren maximal erreichbare Kohärenzzeit ($T_2 \leq 2\,T_1$).

Ein vielversprechendes physikalisches System zur Realisierung von Quantentechnologien, wie Quantenkommunikation, Quanteninformationsverarbeitung und Quantenmetrologie ist das negativ geladene Stickstoff-Fehlstellen Zentrum (NV^-) im Diamanten. Bisher wurde die longitudinale Relaxation der Elektronenspins eines NV^- Ensembles, die durch Spin-Phonon Wechselwirkung getrieben wird nur in Temperaturbereichen höher als $4\,\mathrm{K}$ gemessen.

Diese Arbeit stellt eine Cavity Quantenelektrodynamik Messmethode vor, die es ermöglicht Spin-Phonon Relaxation in einem Temperaturbereich zwischen $25\,\mathrm{mK}$ und $250\,\mathrm{mK}$ zu messen. Wir stellen einen 3D Mikrowellenresonator vor, der es ermöglicht an jeden Spin des Ensembles homogen zu koppeln. Die dispersive Kopplung des Spin Ensembles zum Resonator ermöglicht es uns, die Spin Polarisation indirekt zu messen und so die longitudinale Relaxation zu bestimmen.

Die gemessene maximale $T_1 \approx 8\,\mathrm{h}$ sind ein Indiz für schwache Spin-Phonon Kopplung. Mittels Temperaturscans können wir den direkten Spin-Phonon Prozess als wesentlich für den longitudinalen Zerfall bestimmen. Weiters zeigen wir, dass in einem Temperaturbereich für den $k_B T < \hbar\omega_s$ gilt, T_1 einzig durch die spontane Emission von Spinanregungen in phononische Vakuummoden bestimmt wird.

Schlussendlich vergleichen wir die Messungen meherere Diamantproben um den Einfluss von Gitterschäden auf die longitudinale Relaxation zu untersuchen. Dabei können wir auch zeigen, dass die Messdaten zweier Proben fast das berechnete Relaxationsverhalten eines einzelnen NV^- im perfecten Diamanten wiedergeben.

Contents

x

Chapter 1

Introduction

In 1900, when Max Planck was able to find a description of black body radiation with the introduction of quantized energy [1], the wide physical, technological and philosophical consequences of this discovery were not predictable. This 'Big Bang' of quantum physics paved the way for other game changing discoveries like the description of the photoelectric effect by Albert Einstein [2], the postulation of the Schrödinger equation [3], Heisenberg's principle of uncertainty [4], the relativistic expansion of the quantum theory by Paul Dirac [5] or the development of quantum electrodynamics by Richard Feynmann [6]. All these scientific findings provide an insight into the structure and behaviour of nature and enable applications which were unthinkable before.

Since then, technologies like the laser [7] and the semiconductor based information technologies changed society and living of human significantly. Nowadays, physicists do research on different physical systems to realize quantum computation, the next big step of this technological evolution. Some of the most promising physical systems are artificial atoms [8], trapped ions [9], ultracold neutral atoms [10], Rydberg atoms [11], quantum dots [12] and nitrogen-vacancy center in diamond [13]. However, when we compare all these systems, all show benefits and disadvantages for the realization of a quantum computer.

Within this thesis, we focus on negatively charged nitrogen-vacancy center (NV^-). It is a point defect in diamond, which consists of a carbon substituting nitrogen lattice atom and a neighbouring vacancy. Capturing an additional electron, the NV^- builds a localized spin $S = 1$ system. Due to zero-field splitting, the degeneracy of the ground state is lifted by $2.88\,\mathrm{GHz}$ and the optical transition between the ground state and the

1

first excited state corresponds to 637 nm. These properties enable experiments in the microwave regime and optical read out of the spin state. Therefore, the NV^- becomeas of interest for quantum computation and other applications like magnetic sensing [14] and fluorescence microscope [15].

A crucial parameter for all quantum systems is the longitudinal relaxation rate $\gamma_{||}$, or equvalently the characteristic longitudinal relaxation time T_1. It is a measure for the coupling of the system to its environment and, therefore, a limit for the maximum achievable coherence time $T_2 \leq 2\,T_1$.

So far, T_1 of NV^- was measured to a minimum temperature of 4 K [16, 17]. In this thesis, we present a method to measure the longitudinal relaxation of a NV^- ensemble in a temperature range of 25-300 mK. The ensemble is homogeneously and collectively coupled to a superconducting 3D lumped element microwave resonator and the $\sqrt{N}$ enhancement of the coupling strength is shown (N is the number of spins). Since the resonator is far detuned to the spin transition, the measurement enters the dispersive regime and a quantum non demolition (QND) measurement scheme of the collective spin state is realized. Data for four different NV^- ensemble samples were taken and compared. Furthermore, we determine the basic processes of spin-phonon relaxation and are able to show the limit of T_1 as consequence of spontaneous emission of spin excitations into phononic vacuum modes.

Chapter 2

The negatively charged Nitrogen-Vacancy center in diamond

Among more than hundred known luminescent defects in diamond, the negatively charged nitrogen-vacancy center (NV^-) has such unique properties that it becomes attractive for utilization in quantum technologies [18, 19]. This chapter provides fundamental information about the NV^- center necessary for an understanding of this thesis. First, the crystalline structure of this point defect is discussed. Then electric and magnetic properties are outlined. Good review papers of point defects in diamond and especially NV^- can be found in [20, 13].

2.1 Crystalline Structure

Diamond consists of a face-centred cubic lattice of carbon atoms. The Nitrogen-vacancy center is a point defect of such a lattice, where a carbon atom is substituted with a nitrogen atom and an adjacent lattice vacancy. Nitrogen which has five valence electrons, forms a paramagnetic spin-half system with the vacancy, the neutral NV^0. If the NV^0 captures an additional electron from the lattice, the negatively charged NV^- is created.

The NV axis is orientated along the $\langle 111 \rangle$ crystalline direction and therefore, it has four crystallographical equivalent orientations in diamond. The electronic states of the NV^- are highly localized at the vacancy and the three carbon atoms in nearest-
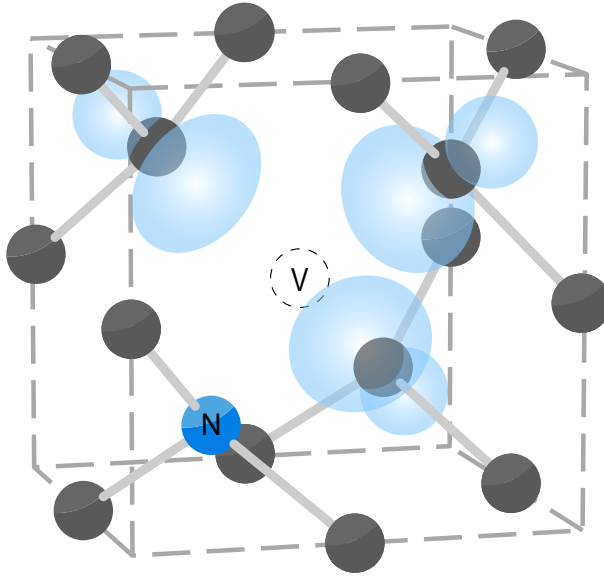
Figure 2.1: **Illustration of the unit cell of diamond containing a NV^-centre.** The NV axis is pointing along the $\langle 111 \rangle$ orientation and the iso-surface of the spin density shown in blue.[21]

neighbour position. Therefore, the NV has a C_{3v} symmetry. Fig. 2.1 shows the unit-cell of diamond containing a NV^- center, illustrating its orientation and symmetry.

The synthesis of such NV^- ensembles is discussed in Sec. 7.2

2.2 Spin properties of the NV^-

The electronic structure of the NV^- center is given by two $S = 1$ triplet states ($^3A_2$, $^3E_2$) and two $S = 0$ singlet states ($^1A_1$,$^1E_1$), which are coupled via inter-system crossing processes (Fig.2.2). Even in the absence of external magnetic or electric fields, the degeneracy of the ground state, the $^3A_2$ triplet state is lifted by the spin-spin interaction of the two unpaired electron spins (dashed box in Fig. 2.2) [22]. This so-called zero-field splitting (ZFS) can be described by the following Hamiltonian:

$$\frac{\hat{H}_{ZFS}}{h} = \mathbf{S}^T \overline{D} \mathbf{S} = D(S_z^2 - \frac{1}{3}\mathbf{S}^2) + E(S_x^2 - S_y^2) \tag{2.1}$$

The zero-field splitting tensor $\overline{D}$ is traceless and, therefore, it is characterized by two fine structure constants D and E. E describes the perturbation of the $m_s = \pm 1$ states caused by the local strain field. This effect is equal to the Stark effect of an external electric field

4

on a NV^- and has a sample dependent strength of a few MHz. Furthermore, D describes the splitting between the $m_s = 0$ and $m_s = \pm 1$ states as measure of the deviation of the electron wave function from spherical symmetry. Hence, $D = 2.88\,\mathrm{GHz}$, this $|0\rangle \leftrightarrow |\pm 1\rangle$ magnetic-dipole transition becomes attractive for coupling to a microwave cavity, enabling cQED experiments like the experiment presented in this thesis or [23] and [24]. For our purpose, E is rather small compared to D and is neglected. Although, the existence of two excited states is significant for calculating the thermal population (see Sec. 7.1).
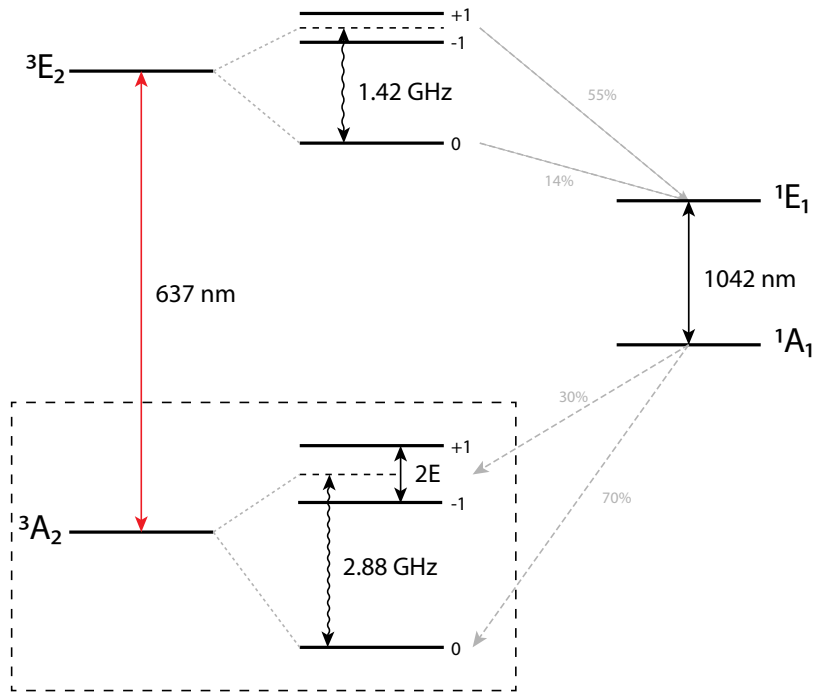
Figure 2.2: **Term scheme of the NV^- center.** In the shaded box is the zero-field splitting of the triplet ground state illustrated. Straight arrows between the triplet and singlet states symbolize electric dipole transitions. Wavy arrows visualize magnetic dipole transitions between sub-levels. Inter-system crossing processes are depicted as dashed grey arrows and the approximate branching ratios from the initial state are given as percentages.

Zeeman splitting, the splitting of spin states due to an static external magnetic field enables to tune the ground state spin transition $|0\rangle \leftrightarrow |\pm 1\rangle$. This interaction is given by

the Hamiltonian,

$$\frac{\hat{H}_Z}{h} = -\mu \mathbf{B}_{ext},\tag{2.2}$$

where μ is the magnetic moment in dependence of the spin $\mathbf{S}$:

$$\mu = g_e \mu_B \mathbf{S}\tag{2.3}$$

Here, $g_e \approx 2$ and $\mu_B \approx 14\,\frac{\text{MHz}}{\text{mT}}$ is the Bohr magneton. Thus, $g_e \mu_B \approx 28\,\frac{\text{MHz}}{\text{mT}}$ is a measure for the energy shift per strength of the applied magnetic field.

Another property of the NV^- is the hyperfine splitting by coupling of the electron spin to Carbon isotopes and impurities present in the diamond. Thereby, the isotopes ^{13}C and ^{14}N are the most prominent. In this thesis hyperfine splitting will not be discussed in detail. Proper papers discussing this topic can be found in [20].

The NV^- ground state has an electric dipole transition to the excited $^3E_2$ triplet state, which has a lifetime of about 10 ns. This so called zero-phonon line (ZPL) corresponds to a wavelength of 637 nm. Another option to excite the NV^- is to drive the ZPL blue-detuned. Surplus energy is emitted to the phonon side band [22], due to the coupling of the $^3E_2$ state to local and global vibrational modes. The advantage of this excitation method is that the bandwidth of the phonon side-band is much larger than the linewidth of the direct transition. Therefore, it is not necessary to lock a excitation laser at the transition frequency and the readout of the spin state is done via detection of the fluorescence of the ZPL. Similar to the $^3A_2$ ground state the degeneracy of the $^3E_2$ state is lifted by ZFS corresponding to 1.42 GHz.

Since electrical dipole transitions are spin conserving, polarization in the $m_s = 0$ state of the NV^- can be reached via inter-system crossing processes between its triplet states and intermediate metastable singlet states, $^1A_1$ and $^1E_1$. The $m_s = \pm 1$ sub-states preferentially decay non-radiative into the $^1E_1$ singlet state, which has a lifetime lower than 1 ns and decays via an electrical dipole transition into the $^1A_1$ state, emitting a photon with a wavelength of 1042 nm. Again, this state decays non-radiative, preferentially into the $m_s = 0$ sub-state of the $^3A_2$ triplet ground state. The whole regime enables to polarize into the $m_s = 0$ ground state with off-resonant optical pumping.

Chapter 3

3D Lumped Element Microwave Resonator

For the readout of the spin ensemble in our experiment, the $3D$ lumped element microwave resonator is essential. The resonant mode has to create an oscillating magnetic field, which interacts with the whole spin ensemble homogeneously.

After an introduction of general properties and the basic two types of microwave resonators, the more complex $3D$ 'bow tie' design is discussed [25]. For further information on microwave resonators and microwave engineering in general [26] can be recommended.

3.1   Fundamentals of Microwave Resonators

In general microwave resonators can be depicted as circuit composed of three fundamental, passive components. The resistor, R, describes the response to current and is a dissipative element. The capacitor, C, stores electric energy in an electric field and causes a negative phase shift between applied voltage and current. In conclusion, the inductor, L, stores electric energy in a magnetic field and causes a positive phase shift between applied voltage and current. (Eq. 3.1) quotes the impedance of the three elements.

$$Z_R = R \qquad\qquad Z_C = \frac{1}{j\omega C} \qquad\qquad Z_L = j\omega L \qquad (3.1)$$

Here, R, C and L are element specific parameter in units, $[R] = \Omega$, $[C] = $ F and $[L] = $ H.

Resonance occurs if a system is periodically stimulated at or close to its eigenfrequency. The excitation energy is stored in different modes of the system, which transfer energy between each other. Without the presence of dissipation processes, resonance would lead to an increasing amplitude and subsequently to a resonance disaster, the collapse of the system.

Resonance of a microwave resonator occurs when the average stored electric and magnetic energy are equal ($W_m = W_e$). The eigenfrequency of the resonator (Eq. 3.2) is dependent to its capacitance and inductance.

$$\omega_0 = \frac{1}{\sqrt{LC}} \tag{3.2}$$

The circuits resistance has not any effect to the eigenfrequency, but is dissipating stored energy. Thus, the energy loss caused by the resistance is $P_{loss} = \frac{1}{2}|I|^2 R$ and the complex input power can be written as

$$P_{in} = \frac{1}{2}Z_{in}|I|^2 = P_{loss} + 2j\omega(W_m - W_e). \tag{3.3}$$

An important characteristic for a resonator is its quality factor Q. It is a measure for the energy dissipation of the resonator (Eq. 3.4), which can be determined with a linewidth ($\Delta\omega$) measurement.

$$Q = \omega\frac{W_{stored}}{P_{loss}} = \omega\frac{W_e + W_m}{P_{loss}} = \frac{\omega_0}{\Delta\omega} \tag{3.4}$$

In experiment, the resonator is coupled to an outer circuit, and, therefore the Q factor of the whole circuit will be lowered. This so called loaded quality factor, Q_L is given by (Eq. 3.5), where Q_i is the quality factor of the resonator and the external Q is Q_e, which is dependent to the external load resistance.

$$\frac{1}{Q_L} = \frac{1}{Q_e} + \frac{1}{Q_i} \tag{3.5}$$

For the description of the coupling strength of a cavity to an external circuit, the coupling coefficient g is defined as:

$$g = \frac{Q_i}{Q_e} \tag{3.6}$$

Three different coupling regimes are distinguishable:

1. Undercouping ($g < 1$): The resonator is weakly coupled to the external circuit, internal losses are dominant.

2. Critical coupling ($g = 1$): The maximum power transfer between resonator and external circuit is achieved by impedance matching.

3. Overcoupling ($g > 1$): The resonator is strongly coupled to the external circuit, external losses are dominant.

Close to resonance, every microwave resonator can be described as neither series nor parallel RLC equivalent circuit. In the following subsection, we discuss basic properties of these two fundamental resonant circuits.

3.1.1 Series Resonant Circuit

The schematic of the basic series RLC resonant circuit is shown in Fig. 3.1.
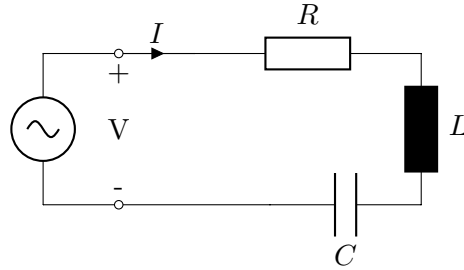
Figure 3.1: **Series RLC circuit**

Following Kirchhoff's circuit laws, the input impedance can be calculated:

$$Z_{in} = R + j\omega L - j\frac{1}{\omega C} \tag{3.7}$$

The average magnetic energy stored in the inductor (W_m) and the average electric energy in the capacitor (W_e) are given by

$$W_m = \frac{1}{4}|I|^2 L \qquad\qquad W_e = \frac{1}{4}|I|^2 \frac{1}{\omega^2 C} \tag{3.8}$$

Note that in resonance, the complex input power (Eq. 3.3) becomes real as well as the input impedance (Eq. 3.7) and Q, which can be calculated with (Eq. 3.4) becomes indirect proportional to R.

$$Q = \frac{\omega_0 L}{R} = \frac{1}{\omega_0 RC} \tag{3.9}$$

Furthermore, we want to determine the input impedance near the circuits resonance. Therefore, we let $\omega = \omega_0 + \Delta\omega$, where $\Delta\omega$ is small and get

$$Z_{in} \simeq R + j2L\Delta\omega = R + j\frac{2RQ\Delta\omega}{\omega_0}. \tag{3.10}$$

An detailed derivation of (Eq. 3.10) can be found in [26].

3.1.2 Parallel Resonant Circuit

The schematic of the basic parallel RLC resonant circuit is shown in Fig. 3.2.
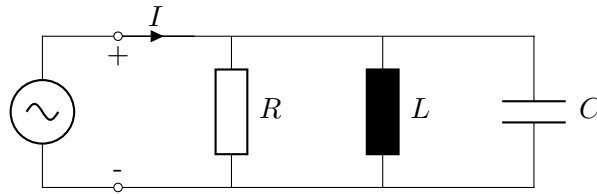
Figure 3.2: **Parallel RLC circuit**

$$Z_{in} = (\frac{1}{R} + \frac{1}{j\omega L} + j\omega C)^{-1} \tag{3.11}$$

The average magnetic energy stored in the inductor (W_m) and the average electric energy in the capacitor (W_e) are given by

$$W_e = \frac{1}{4}|V|^2 C \qquad\qquad W_m = \frac{1}{4}|V|^2 \frac{1}{\omega^2 L}. \tag{3.12}$$

Similar to the series circuit, the complex input power (Eq. 3.3) and the input impedance (Eq. 3.11) become real when resonance occurs. However, the parallel circuits Q differs from the series circuits Q and is direct proportional to R.

$$Q = \frac{R}{\omega_0 L} = \omega_0 RC \tag{3.13}$$

Again, we evaluate the input impedance near the circuits resonance, where $\Delta\omega$ is small, to give

$$Z_{in} \simeq \frac{R}{1 + 2j\Delta\omega RC} = \frac{R}{1 + 2jQ\Delta\omega/\omega_0}. \tag{3.14}$$

Like for the series circuit, an detailed derivation of (Eq. 3.14) can be found in [26].

3.2 Bow Tie Resonator

As mentioned in the introduction of this chapter, interaction of a cavity with the spin ensemble enables readout and also manipulation of the spin state (see Sec. 4.3.3). Therefore, the resonance frequency of the cavity has to match the NV^- spin transition of 2.88 GHz. For a collective, coherent coupling of the spins to the cavity, the resonant cavity mode has to generate a homogeneous magnetic field in the area, where the diamond is placed.

(a)

(b)

(c)

(d)
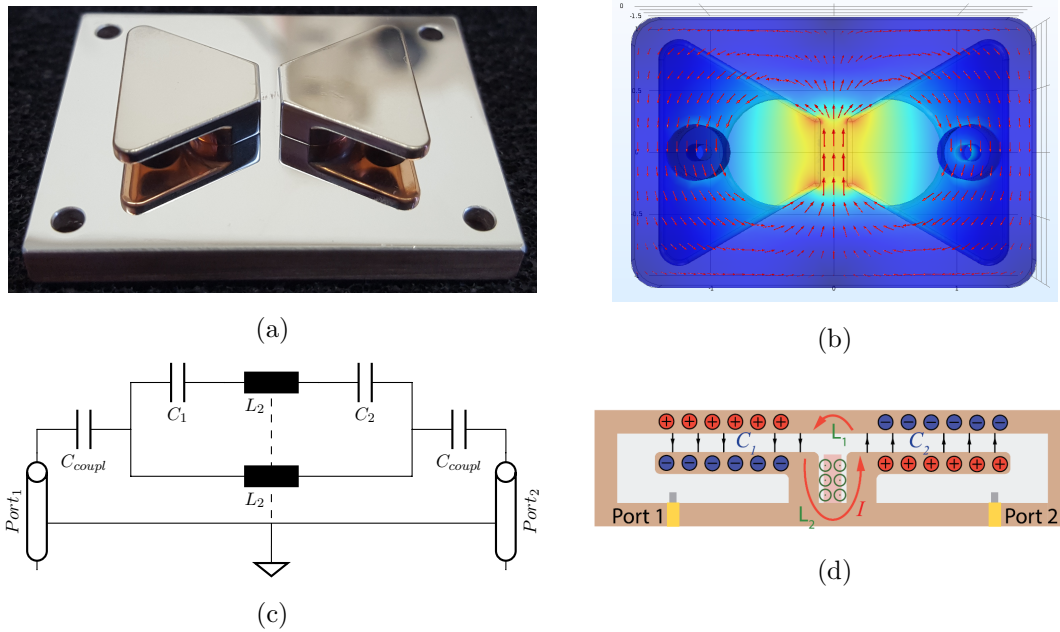
Figure 3.3: (a) Manufactured aluminum "Bow Tie" resonator. For illustrative purpose, frame and top lid were removed. (b) Simulated results of the magnetic field for the resonant mode used in experiment. Red and blue indicate zones of high and low magnetic field density. The magnetic field gets focused in the probe volume in the center of the cavity. (Image taken from [27] (c) Equivalent circuit of the 3D lumped microwave resonator. (d) Schematic cross section of the cavity perpendicular to the mode direction. Black arrows symbolize the electric field and red arrows symbolize the current, inducing a magnetic field (green circles), generated by the resonant mode. (Image taken from [25])

To meet these requirements, we came up with an resonator design, where two bow-tie

shaped structures are place in the center of a closed box (Fig. 3.3a). The top surface of each bow tie builds a capacitor with the lid. In resonance, a current at the bow tie surface and a counter-propagating current at the lid surface are oscillating between these capacitors, generating a focused homogeneous magnetic field in the cavity center (Fig. 3.3b).

Figure 3.3c shows the equivalent circuit of our cavity which can be transformed to a equivalent parallel resonant circuit with $\omega_0 = \frac{1}{\sqrt{L_{tot}C_{tot}}}$.

$$C_{tot} = \frac{C_1 C_2}{C_1 + C_2} = \frac{C}{2} = \frac{2\epsilon_0 A}{d} \tag{3.15}$$

$$L_{tot} = L_1 + L_2 \approx l \ln\left(\frac{l}{w+t}\right) + 0.2235\left(\frac{l}{w+t}\right) + 0.5 \tag{3.16}$$

If we consider (Eq. 3.15) and (Eq. 3.16), it is obvious that ω_0 is solely dependent to the cavity geometry and material. In (Eq. 3.15), A is the top area of one bow tie, d is the separation between bow tie and top lid and ϵ_0 is the dielectric constant. (Eq. 3.16) shows that L_{tot} can be approximated by the inductance of a flat wire conductor [28], where l is the current-carrying length, w the current width and t is the skin depth of the oscillating current.

The cavity is capacitively coupled to a outer measurement circuit via two coaxial ports below the bow ties. The coupling regime can be tuned with the length of the couplers (grey spikes in Fig. 3.3d).

To increase the sensitivity of the measurement, the Q factor has to be as high as possible. Therefore, the cavity was manufactured from aluminium, a type I superconductor with a highest transition temperature, $T_C = 1.20\,\text{K}$. As a result, $Q = 517000$ was measured with an empty cavity and $1.5\,\text{mm}$ coupler at $100\,\text{mK}$. Detailed information about the resonator, used in experiment can be found in (see Sec. 7.3).

Note that design and fabrication of these resonators was not done within this thesis, the reader is referred to [25] and the project thesis of Daniel Wirtitsch [27] for further and detailed information.

Chapter 4

Cavity QED

This chapter gives an introduction into the theoretical description of the in this thesis presented experiment. First, we discuss the quantum mechanical description of the two-level system and the quantized electromagnetic field. Second, introduce the Jaynes-Cummings model to describe the two-level system-field interaction. We expand this model for an ensemble of two-level systems to the Tavis-Cummings model and derive the dispersive regime, which enables quantum non-demolition measurements. Conclusively, we outline origins for non-unitary dynamics.

For a deeper introduction and more details on the concepts of quantum optics the author recommends [29, 30, 31].

4.1 The two-level quantum system

An exact description of the interaction of any real quantum systems with electromagnetic fields is impossible. However, the simplification of such systems to the simplest quantum system, the two-level system is useful and enables the study of fundamental effects.

The two-level system consists of two non-degenerate eigenstates $|i\rangle$, $(i = a, b)$ with the eigenvalues

$$\hat{H}_0 |i\rangle = \hbar\omega_i |i\rangle.$$ (4.1)

In its eigenbasis, the Hamiltonian is depicted as

$$\hat{H}_0 = \sum_{i=a,b} \hbar\omega_i \sigma_i = \begin{bmatrix} \hbar\omega_a & 0 \\ 0 & \hbar\omega_b, \end{bmatrix}$$ (4.2)

where $\sigma_i = |i\rangle\langle i|$ are the projection operators, which describe the population probabilities for each level.

Further, we introduce the Pauli operator

$$\sigma_z = \sigma_a - \sigma_b, \tag{4.3}$$

which describes the population inversion of the system. Thus, we can rewrite the Hamiltonian as

$$\hat{H}_0 = \sum_{i=a,b} \left(\frac{1}{2}\hbar\omega_i\sigma_i + \frac{1}{2}\hbar\omega_{ab}\sigma_z \right), \tag{4.4}$$

with the transition frequency $\omega_{ab} = \omega_a - \omega_b$. For further simplification we set the zero point energy in between of $\hbar\omega_a$ and $\hbar\omega_b$ to get

$$\hat{H}_0 = \frac{1}{2}\hbar\omega_{ab}\sigma_z \tag{4.5}$$

with the eigenvalues $\langle \hat{H}_0 \rangle = \pm\frac{1}{2}\hbar\omega_{ab}$.

To conclude, we define the raising and lowering operators in dependence of the Pauli operators.

$$\sigma_+ = \frac{1}{2}(\sigma_x + i\sigma_y) \qquad\qquad \sigma_- = \frac{1}{2}(\sigma_x - i\sigma_y) \tag{4.6}$$

4.2 Electromagnetic field

4.2.1 The classical free electromagnetic field

For the description of the free electromagnetic field, we have to apply the source free Maxwell equations:

$$\mathbf{div\,E} = 0 \qquad \mathbf{div\,B} = 0 \qquad \mathbf{rot\,E} = -\frac{\partial\mathbf{B}}{\partial t} \qquad \mathbf{rot\,B} = \frac{\partial\mathbf{E}}{\partial t} \tag{4.7}$$

The second and third of Maxwell's equation define the $\mathbf{B}$ and $\mathbf{E}$ field with the gauge free vector potential $\mathbf{A}$:

$$\mathbf{B} = \nabla \times \mathbf{A} \qquad\qquad \mathbf{E} = -\frac{\partial\mathbf{A}}{\partial t} \tag{4.8}$$

By applying the Coulomb gauge condition $\partial\mathbf{A} = 0$ and substitute (Eq. 4.8) into the the fourth of Maxwell's equations, we obtain the differential equation

$$\nabla^2\mathbf{A} - \frac{1}{c^2}\frac{\partial^2\mathbf{A}}{\partial t^2} = 0, \tag{4.9}$$

with the solution [31]

$$\mathbf{A}(\mathbf{r}, t) = \int_\mathbf{k} \sum_{\alpha=1,2} \sqrt{\frac{\hbar}{2\omega_k \epsilon_0 V}} \pi_{\alpha,k} \Big[A_{k,\alpha} e^{i(\mathbf{k} \cdot \mathbf{r} - \omega_k t)} + c.c. \Big] d\mathbf{k}. \tag{4.10}$$

Here, we integrate over the continuous wave vectors $\mathbf{k}$ and the sum takes both orthogonal polarization modes π_α into account. V is the mode volume, ω_k the eigenfrequency of the mode $\mathbf{k}$, ϵ_0 is the dielectric constant and $A_{k,\alpha}$ a dimensionless complex amplitude. To obtain $\mathbf{B}$ and $\mathbf{E}$, (Eq. 4.10) is substituted into (Eq. 4.8).

The total energy of the free multi mode electromagnetic field is given by the Hamiltonian

$$H = \frac{1}{2} \int (\epsilon_0 \mathbf{E}^2 + \frac{1}{\mu_0} \mathbf{B}^2) dr. \tag{4.11}$$

4.2.2 Second Quantization / Fock state

To study the electromagnetic field in a cavity, we consider an electromagnetic field enclosed by a box with reflecting walls. This boundary condition leads to discrete standing waves as solution for the electromagnetic field. Therefore, the integral in (Eq. 4.10) becomes a discrete sum. Furthermore, the vector potential $\mathbf{A}$ is quantized and the amplitude $A_{k,\alpha}$ is substituted with the bosonic creation operator $a^\dagger$ and annihilation operator a.

$$\mathbf{A}(\mathbf{r}, t) = \sum_{k,\alpha} \sqrt{\frac{\hbar}{2\omega_k \epsilon_0 V_{mode}}} \pi_{k,\alpha} \Big[a_k e^{i(\mathbf{k} \cdot \mathbf{r} - \omega_k t)} + a_k^\dagger e^{-i(\mathbf{k} \cdot \mathbf{r} - \omega_k t)} \Big] \tag{4.12}$$

The boson commutation relations are given by

$$[a_k, a_{k'}] = [a_k^\dagger, a_{k'}^\dagger] = 0 \qquad\qquad [a_k, a_{k'}^\dagger] = \delta_{kk'}. \tag{4.13}$$

The relations in (Eq. 4.8) and (Eq. 4.12) are used to calculate the quantized solutions of the electric and magnetic fields. For the evaluation of the Hamiltonian of the quantized electromagnetic field we insert these solutions in (Eq. 4.11). With the bosonic commutation relations the Hamiltonian reduces to

$$H = \sum_k \hbar \omega_k \Big(a_k^\dagger a_k + \frac{1}{2} \Big), \tag{4.14}$$

where $a_k^\dagger a_k$ is the number of photons in the mode $\mathbf{k}$ and $\frac{1}{2}\hbar\omega_k$ is the zero point energy of the mode. Each mode can be described as independent harmonic oscillator.

The eigenstates $|n_k\rangle$ of this Hamiltonian are also eigenstates of the number operator $N_k = a_k^\dagger a_k$ and are known as Fock states.

$$a_k^\dagger a_k |n_k\rangle = n_k |n_k\rangle \tag{4.15}$$

When we apply the creation or annihilation operator on a Fock state we get

$$a_k |n_k\rangle = \sqrt{n_k} |n_k - 1\rangle \qquad\qquad a_k^\dagger |n_k\rangle = \sqrt{n_k + 1} |n_k + 1\rangle, \tag{4.16}$$

where $a_k^\dagger$ adds one quantum of excitation to the system in contrast to the removal of an excitation by a. Furthermore, the nth excited state can be generated by applying $a_k^\dagger$ on the ground state $|0\rangle$ n-times.

$$|n_k\rangle = \frac{\left(a_k^\dagger\right)^{n_k}}{\sqrt{n_k!}} |0\rangle \tag{4.17}$$

Since the Fock states are orthogonal, complete and can be normalized, they built a complete set of basis vectors for the Hilbert space.

4.3 The Jaynes-Cummings model

The Jaynes-Cummings model [32] describes the interaction of a single two level quantum system with a quantized electromagnetic field of a cavity. The Hamiltonian is given by

$$\hat{H} = \hat{H}_{field} + \hat{H}_{2level} + \hat{H}_{int}, \tag{4.18}$$

where $\hat{H}_{field}$ is the Hamiltonian of the free electromagnetic field, the second term describes the two level system and $\hat{H}_{int}$ is the interaction Hamiltonian.

4.3.1 The dipole approximation

Since the size of the two level system is considered to be orders of magnitude smaller than the wavelength of the electromagnetic field, we can neglect the gradient of the field amplitude and allows us to model H_{int} as a dipole interaction. The interaction Hamiltonian has the form:

$$\hat{H}_{int} = -\mu_s \mathbf{B}(t). \tag{4.19}$$

We consider an electron as source of the magnetic dipole moment $\mu_s = g_e \mu_B \frac{\mathbf{S}}{\hbar}$, where $g_e \approx 2$ is the gyromagnetic factor, μ_B is the Bohr magneton and $\mathbf{S}$ the spin vector. Note that a magnetic field in quantization axis would lead to a Zeeman splitting [30] and only

magnetic field components of this quantization axis lead to level mixing. However, $\hat{H}_{int}$ for an in x-direction polarized magnetic field $B_x = B_0(a + a^\dagger)$ is given by

$$\hat{H}_{int} = -\hbar \frac{g_e \mu_B}{2} \sigma_x B_x = -\hbar g_0 (\sigma^+ + \sigma^-)(a + a^\dagger) \tag{4.20}$$

Here, g_0 is a constant dependent on the magnetic dipole moment and on the magnetic field amplitude which describes the coupling strength of the two level system to the cavity.

4.3.2 The rotating wave approximation

For studying the system dynamics we transform the operators in (Eq. 4.20) to the interaction picture and get

$$\sigma^\pm(t) = \sigma^\pm e^{\pm i \omega_{ab} t} \qquad a(t) = a e^{-i \omega_k t} \qquad a^\dagger(t) = a^\dagger e^{i \omega_k t}. \tag{4.21}$$

We substitute these time dependent operators in Eq.4.20 to obtain the interaction Hamiltonian in the interaction picture:

$$\hat{H}_{int}(t) = -\hbar g_0 \Big(\sigma^- a e^{-i(\omega_{ab}+\omega_k)t} + \sigma^+ a e^{i(\omega_{ab}-\omega_k)t}$$
$$+ \sigma^- a^\dagger e^{-i(\omega_{ab}-\omega_k)t} + \sigma^+ a^\dagger e^{i(\omega_{ab}+\omega_k)t} \Big) \tag{4.22}$$

All four terms in the parenthesis represent different processes:

- $\sigma^- a$: Each subsystem, the cavity and the two-level system emits a photon, this process is non energy conserving.

- $\sigma^+ a$: The two-level system absorbs a cavity photon and gets excited. Hence, the excitation number of the whole system is conserved, this process is unitary and the total energy conserved.

- $\sigma^- a^\dagger$: The two-level system emits a photon which is absorbed by the cavity. This also is a unitary process and the total energy is conserved.

- $\sigma^+ a^\dagger$: This process describes the excitation of both, the cavity and the two-level system. Like the first process, this process is non energy conserving because two excitations are added to the system.

In the regime of our interest, where $\omega_k \approx \omega_{ab}$, the amplitudes of the non energy conserving processes oscillate fast compared to the slowly varying amplitudes of the unitary processes. If $g_0 \ll \omega_{ab}$, we can neglect these fast oscillating processes. This well-known approximation is called rotating wave approximation and leads to the interaction Hamiltonian

$$\hat{H}_{int} = -\hbar g_0 \left(\sigma^+ a + \sigma^- a^\dagger \right) \tag{4.23}$$

and the Jaynes-Cummings Hamiltonian of the total system

$$\hat{H}_{JC} = \frac{1}{2} \hbar \omega_{ab} \sigma_z + \hbar \omega_c a^\dagger a - \hbar g_0 \left(\sigma^+ a + \sigma^- a^\dagger \right). \tag{4.24}$$

The first term in (Eq. 4.24) is the undisturbed Hamiltonian of the two-level system and the second term is the Hamiltonian of a single mode cavity with eigenfrequency ω_c.

4.3.3 Dispersive regime

In the following sector we want to study the previously discussed system in the dispersive regime, where the detuning of the cavity eigenfrequency from the transition frequency of the spin system is much larger than the coupling strength between these systems ($\Delta = \omega_{ab} - \omega_c \gg g_0$). We apply an unitary transformation to the Jaynes-Cummings Hamiltonian [33]

$$\hat{H}_{disp} = \hat{U}^\dagger \hat{H}_{JC} \hat{U} \tag{4.25}$$

with

$$\hat{U} = e^{-\frac{g_0}{\Delta}(\sigma^- a^\dagger - \sigma^+ a)}. \tag{4.26}$$

Since an exponential function can be written as power series, we can rewrite an unitary transformation as

$$e^{\hat{A}} \hat{B} e^{-\hat{A}} = \hat{B} + [\hat{A}, \hat{B}] + \frac{1}{2} [\hat{A}, [\hat{A}, \hat{B}]], \tag{4.27}$$

neglecting higher than second order terms. By making use of the commutation relation for boson operators and Pauli matrices (Eq. 4.28 and Eq. 4.29) this expansion yields to an Hamiltonian given in (Eq. 4.30).

$$[a, a^\dagger a] = a \qquad\qquad [a^\dagger, a^\dagger a] = -a^\dagger \tag{4.28}$$

$$[\sigma^\pm, \sigma^\mp] = \pm \sigma_z \qquad [\sigma^\pm, \sigma_z] = \mp 2\sigma_z \qquad \sigma^\pm \sigma^\mp = \frac{1}{2}(\mathbb{1} \pm \sigma_z) \tag{4.29}$$

$$\hat{H}_{disp} = \Big(\frac{\omega_{ab}}{2} + \frac{g_0^2}{2\Delta}\Big)\sigma_z + \Big(\omega_c + \frac{g_0^2}{\Delta}\sigma_z\Big)a^\dagger a + \frac{g_0^2}{2\Delta}\mathbb{1} \qquad (4.30)$$

When we compare the Hamiltonian for the dispersive regime with the Jaynes-Cummings Hamiltonian (Eq.4.24) it becomes obvious that the two subsystems can not exchange excitations anymore due to the missing interaction term. However, the resonance of the two-level system is tuned and increases by $\frac{g_0^2}{\Delta}$ and the cavity obtains a shift dependent to the spin state. This dependence is crucial for many QED experiments [18, 34] since it enables a indirect and quantum non demolition (QND) measurement of the spin state [35]. The fourth term is an energy offset and can be neglected.

4.4 The Tavis-Cummings model

For a proper description of an ensemble of NV^- center interacting with a cavity mode, we have to consider collective effects. As Dicke showed in 1954 [36], an ensemble of molecules or atoms interacting with a radiation field has to be described as single quantum system to explain coherent processes in spontaneous emission. The Dicke model is valid if our system fulfils the following requirements:

- The mode volume of the radiation field is large compared to the expansion of the molecule or atom ensemble.

- All emitters are indistinguishable.

- The wavefunctions of the emitters do not overlap, dipole-dipole interaction can be neglected.

- Coherence occurs due to the coupling of the emitters to the same radiation field.

For further information about recent developments of the Dicke model we can recommend [37].

However, the Dicke model is a semiclassical model and does not consider a quantized electromagnetic field. This extension was made by Tavis and Cummings [38, 39]. N two-level systems are coupled via magnetic or electric dipole interaction to a single-mode of the quantized electromagnetic field. For this system, the so called Tavis-Cummings Hamiltonian is given by

$$\hat{H}_{TC} = \hbar\omega_c a^\dagger a + \frac{1}{2}\hbar\omega_{ab}\sum_{i=1}^{N}\sigma_z^{(i)} - \hbar\sum_{i=1}^{N}g_{(i)}\big(\sigma_+^{(i)}a + \sigma_-^{(i)}a^\dagger\big). \qquad (4.31)$$

4.4.1 Tavis-Cummings in terms of the collective spin

In the following we assume that the coupling strength g_i is homogeneous for all two-level systems ($g_i = g_0$). Furthermore, we introduce the collective spin $\mathbf{S} = (S_x, S_y, S_z)^T$ with the operators, given by

$$S_z = \frac{1}{2N} \sum_{i=1}^{N} \sigma_z^{(i)} \qquad\qquad S_\pm = \frac{1}{\sqrt{N}} \sum_{i=1}^{N} \sigma_\pm^{(i)} \qquad (4.32)$$

and their commutation relations, given by

$$[S^\pm, S^\mp] = \pm 2S_z \qquad\qquad [S_z, S^\pm] = \pm S^\pm. \qquad (4.33)$$

These assumptions allow to rewrite the Hamiltonian in the following form:

$$\hat{H}_{TC} = \hbar\omega_c a^\dagger a + \hbar N \omega_{ab} S_z - \hbar\sqrt{N} g_0 \left(S_+ a + S_- a^\dagger\right) \qquad (4.34)$$

When we compare this result with Eq. 4.24, we see that the effective coupling between the collective spin and the cavity mode scales with $g_{eff} = \sqrt{N} g_0$.

This scaling of the coupling strength is crucial for cQED experiments with NV^- in the microwave regime. The coupling strength of the NV^- to the external magnetic field of the microwave cavity with bow tie design is $g_0 \approx 30 - 70\,\mathrm{mHz}$ and, therefore, too weak to resolve the coupling of a single NV^-. Nevertheless, this collective effect enables experiments with NV^- ensembles, as presented in this thesis.

4.4.2 Eigenstates of the Tavis-Cummings model

To determine the eigenstates of the Tavis-Cummings Hamiltonian, we consider the eigenstates of the subsystems, the spin ensemble and the cavity.

The eigenstates of the cavity, the so called Fock states were already discussed in Sec. 4.2.2.

Eigenstates of the spin ensemble are called Dicke states and are denoted with $|S, M\rangle$. These states are simultaneously eigenstates of the $\hat{S}^2$ and the $\hat{S}_z$ operators with the eigenvalues

$$\hat{S}^2 |S, M\rangle = S(S+1) \qquad\qquad \hat{S}_z |S, M\rangle = M |S, M\rangle, \qquad (4.35)$$

and are degenerate by $\frac{(2S+1)N!}{(N/2+S+1)!(N/2-S)!}$. The quantum numbers S and M can reach values of $0 \leq S \leq \frac{N}{2}$ and $-S \leq M \leq S$.

Within the Tavis-Cummings model the collective spin is conserved because of $[\hat{S}^2, \hat{H}_{CT}] = 0$. Therefore, we can chose the product states of Dicke and Fock states as basis for the Tavis-Cummings Hamiltonian. Another useful parameter of the given system is the excitation number $n^* = M + n$, which sums up the excitations of the spin ensemble and the cavity. The excitation number operator $(\hat{S}_z + a^\dagger a)$ also commutes with $\hat{H}_{TC}$ and the excitation number is conserved.

In order to illustrate the Tavis-Cummings model, we give an example of a system with one excitation ($n^* = 1$). We will denote the ground Fock state as $|0\rangle$ and the excited Fock state as $|1\rangle$. In the ground state of the spin system, all single spins are polarized and we can write this state as

$$|\psi_0\rangle = |\downarrow, \downarrow, ..., \downarrow\rangle. \tag{4.36}$$

The wavefunction of spin ensemble with one excitation is given by the fully symmetric Dicke state [36],

$$|\psi_1\rangle = \frac{1}{\sqrt{N}} \sum_{i=1}^{N} |..., \downarrow, \uparrow_i, \downarrow, ...\rangle. \tag{4.37}$$

If there is no interaction, the product states $|\Psi_1\rangle = |1\rangle \otimes |\psi_0\rangle$ and $|\Psi_2\rangle = |0\rangle \otimes |\psi_1\rangle$ are the degenerate eigenstates of the system. When interaction is present, the degeneracy is lifted, and the two product states are mixing and generate two eigenstates with energies given by

$$E_\pm = \hbar \frac{\omega_c + \omega_{ab}}{2} \pm \frac{\hbar}{2} \sqrt{4N g_0^2 + \Delta^2}. \tag{4.38}$$

In the case of resonance ($\omega_c = \omega_{ab}$) we see that the degeneracy is lifted by $\Delta E = \sqrt{N} g_0$ and like in (Eq. 4.34) the coupling scales with the square root of the ensemble size.

When we reduce the ensemble size to $N = 1$, but allow higher excitations n^* we gain the eigenvalues of the Jaynes-Cummings Hamiltonian:

$$E_\pm = \hbar n^* \omega_c \pm \hbar \sqrt{(n^* + 1)} \tag{4.39}$$

For each excitation exist two eigenstates which are separated by an energy that scales with $\sqrt{n^* + 1}$.

Fig 4.1 compares the previously discussed models and illustrates the splitting of the excitation eigenstates and the scaling of this splitting.
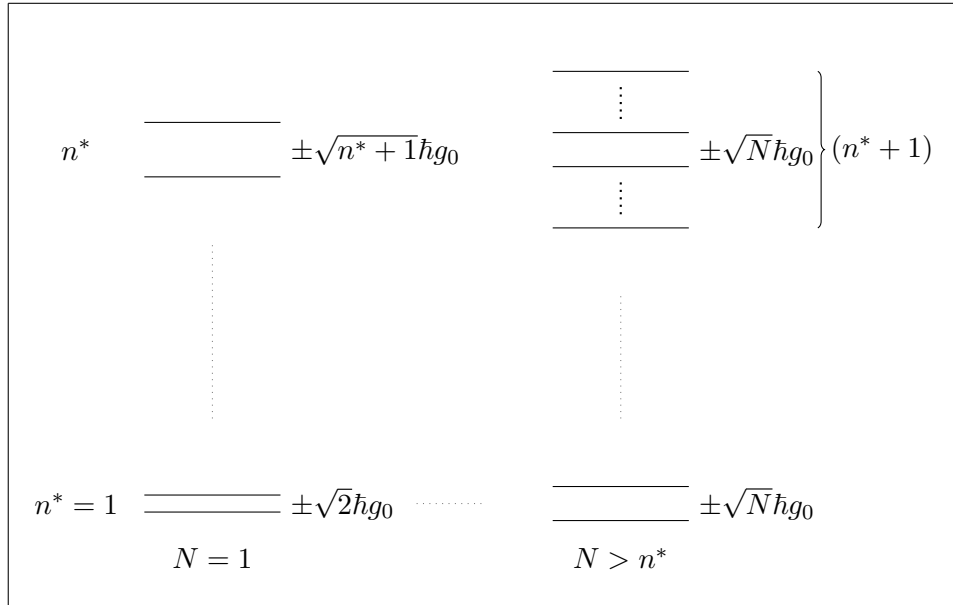
21

Figure 4.1: **Comparison of the Tavis-Cummings model and the Jaynes-Cummings model on resonance.** The left hand side illustrates the eigenstates of the Jaynes-Cummings model. The system has two eigenstates per excitation n^* which are separated by an energy which scales with the square root of n^* and g_0. On the right hand side the eigenstates of the Tavis-Cummings model are shown in a regime where the excitation number is small compared to the ensemble size. The energy separation of the eigenstates per excitation scales with the square root of the ensemble size. Furthermore, the system has $n^* + 1$ eigenstates for n^* excitations.

4.4.3 Tavis-Cummings in dispersive regime

Similar to the Jaynes-Cummings Hamiltonian (see Eq. 4.30), the Tavis-Cummings Hamiltonian can be transformed into the dispersive regime. The applied transformation has to be adjusted slightly because it has to consider collective effects:

$$\hat{U} = e^{\frac{g_0 \sqrt{N}}{\Delta}(S^- a^\dagger - S^+ a)} \tag{4.40}$$

The expansion of the unitary transformation (see Eq. 4.27), the commutation relations for bosons (see Eq. 4.28) and the commutation relations for the collective spin (see

Eq. 4.33) yield the Hamiltonian:

$$\hat{H}_{disp} = \left(\omega_{ab} + \frac{Ng_0^2}{\Delta}\right)S_z + \left(\omega_c + \frac{2Ng_0^2}{\Delta}S_z\right)a^\dagger a \tag{4.41}$$

This allows us to measure the spin state via spectroscopy of the cavity indirectly, as a QND measurement.

4.5   Non-Unitary dynamics

In the final part of this theory chapter we want to discuss the influence of non-unitary processes on our system. Thus far, we described the system as closed system where the energy is conserved and its time evolution is unitary. However, real systems are coupled to an environment which gives rise to dissipative processes.

We want to develop a theory which is capable to describe the dynamics of parameters of the in experiment observed system. We can apply the Tavis-Cummings model for the description of a NV^- ensemble coupled to a cavity mode, even though we have to add a term to include the external cavity probe field. We can write down the Hamiltonian.

$$\hat{H}_{Sys} = \hbar\omega_c a^\dagger a + \hbar\omega_s S_z^2 - \hbar g_{eff}(S^+ a + S^- a^\dagger) + \hbar\eta(a^\dagger e^{-i\omega_d t} + a e^{i\omega_d t}) \tag{4.42}$$

Where η is the probe field amplitude, ω_d is the probe field frequency and $S_z^2 = \frac{1}{N}\sum_j^N \sigma_{z,j}^2$ is the measure of the spin polarization which takes the $m_s = \pm 1$ degeneracy of the excited NV^- triplet state into account. Next, we transform into the rotating frame with the unitary transformation operator

$$\hat{U} = e^{-i\omega_d(a^\dagger a + S_z^2)} \tag{4.43}$$

which yields the Hamiltonian with the detunings $\Delta_s = \omega_s - \omega_d$ and $\Delta_c = \omega_c - \omega_d$:

$$\hat{H} = \hbar\Delta_c a^\dagger a + \hbar\Delta_s S_z^2 - \hbar g_{eff}(S^+ a + S^- a^\dagger) + \hbar\eta(a^\dagger + a) \tag{4.44}$$

This transforms the probe field term in (Eq. 4.42) into the frame of the ensemble-cavity system.

Furthermore, we define ρ as the density operator of the complete system and we can describe the dynamics of the system with the Liouville equation [40]:

$$\frac{d}{dt}\rho = -\frac{i}{\hbar}[\hat{H}, \rho] \tag{4.45}$$

However, this equation still describes an unitary evolution. To introduce non-unitary processes we expand the Liouville equation with Lindblatt terms ($\mathcal{L}$) and get the master equation [40],

$$\frac{d}{dt}\rho = -\frac{i}{\hbar}[\hat{H}, \rho] + \sum_k \mathcal{L}_k. \tag{4.46}$$

4.5.1 Lindblatt terms of the driven spin ensemble-cavity system

Each Lindblatt term describes a certain loss channel mediated by the system-environment interaction. For the given system, three processes are essential:

- **Longitudinal relaxation**

  Longitudinal relaxation occurs when energy determining system parameters (e.g. collective spin) decay and energy is dissipated. It can be mediated via spontaneous emission or other processes, that are dependent on the phase state of the system, like spin-lattice relaxation in solid states. The Lindblatt term of such processes can be written as

  $$\mathcal{L}_{long}(\rho) = \gamma_{||}(2S^-\rho S^+ - S^+S^-\rho - \rho S^+S^-), \tag{4.47}$$

  where $\gamma_{||}$ is the relaxation rate and the inverse of the characteristic relaxation time T_1. Furthermore, $2T_1$ is the ultimate limitation for coherence in quantum systems [41].

- **Homogeneous broadening:**

  The term describing processes which lead to a destruction of the phase of a quantum state is given by

  $$\mathcal{L}_{hom}(\rho) = \gamma_\perp(2S_z^2\rho S_z^2 - S_z^2\rho - \rho S_z^2). \tag{4.48}$$

  The relaxation rate $\gamma_\perp$ and its inverse T_2 are measures for the coherence of a quantum system. An example for such a decoherence process is spin-spin interaction of a qubit with its local spin environment.

  In this context, inhomogeneous broadening and its characteristic time T_2^* should also be mentioned. It describes the distribution of the intrinsic resonance frequency in an emitter ensemble and leads to dephasing, although it is unitary. However, this process is not modelled with (Eq. 4.48), but rather included in the summation over all spins in (Eq. 4.31).

- **Cavity damping:**

  The lifetime of a photon in a cavity is limited by the coupling to the environment and internal losses. These losses can be described with the Lindtblatt term,

  $$\mathcal{L}_{cav}(\rho) = \kappa(2a\rho a^\dagger - a^\dagger a\rho - \rho a^\dagger a). \tag{4.49}$$

  Here, κ is the cavity loss rate given as the half width half maximum of the cavity. Its inverse is the photon lifetime in the cavity.

  For microwave cavities, sources of internal losses are e.g. ohmic dissipation, RF losses in the superconducting phase and the coupling to the environment is determined by the length of the microwave coupler.

4.5.2 Dynamics of observables

In general, the equation of motion of the expectation value of an operator is given by [29]

$$\langle\dot{O}\rangle = Tr(O\dot{\rho}). \tag{4.50}$$

We can use this formula and (Eq. 4.46) to derive the equations of motion of the in (Eq. 4.44) occurring operators.

$$\langle\dot{a}\rangle = -i\Delta_c\langle a\rangle - ig_{eff}\langle S^-\rangle - \kappa\langle a\rangle + \eta \tag{4.51}$$

$$\langle\dot{S^-}\rangle = -i\Delta_s\langle S^-\rangle - 2ig_{eff}\langle a\rangle + 3ig_{eff}\langle a\rangle\langle S_z^2\rangle - (\gamma_\perp^* + 2\gamma_{||})\langle S^-\rangle \tag{4.52}$$

$$\langle\dot{S_z^2}\rangle = -ig_{eff}\left(\langle a\rangle\langle S^+\rangle - \langle a^\dagger\rangle\langle S^-\rangle\right) - 2\gamma_{||}\langle S_z^2\rangle \tag{4.53}$$

Note that the equations of motion for $\langle a^\dagger\rangle$ and $\langle S^+\rangle$ are given by the complex conjugate of (Eq. 4.51) and (Eq. 4.52).

In experiment we measure the transmission of the drive field through the cavity, which is proportional to $\langle a^\dagger a\rangle$. To derive an expression for this operator we consider a steady state of the system and set the equations of motion to zero. Now, we use (Eq. 4.52) to find an expression for $\langle S^-\rangle$ yielding a term for $\langle a\rangle$. Its square of the absolute value is given by

$$\langle a^\dagger a\rangle = \frac{\eta^2}{\left(\kappa + \frac{g_{eff}^2(2-3\langle S_z^2\rangle)(2\gamma_{||}+\gamma_\perp)}{(2\gamma_{||}+\gamma_\perp)^2+\Delta_s^2}\right)^2 + \left(\Delta_c + \frac{g_{eff}^2\Delta_s(2-3\langle S_z^2\rangle)}{(2\gamma_{||}+\gamma_\perp)^2+\Delta_s^2}\right)^2}. \tag{4.54}$$

We see that the transmission is Lorentzian shaped and compared to an empty cavity, the resonance frequency and the half-width of half-maximum is modulated by the spin

ensemble. The dependence on $\gamma_{||}$ and $\gamma_\perp$ leads to a broadening of the Lorentzian and a reduced maximum shift of the resonance frequency (Fig. 4.2).
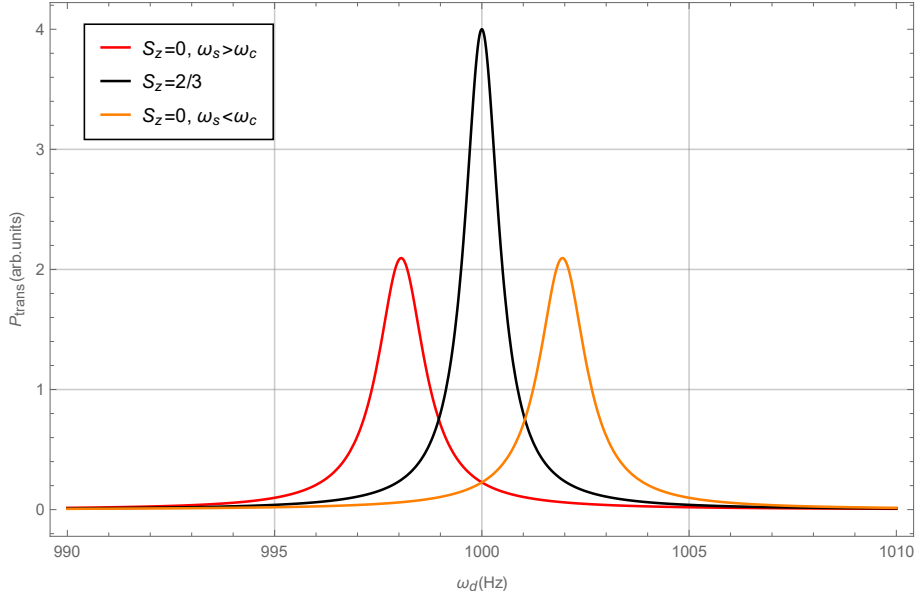

Figure 4.2: **Simulated transmission spectra of a cavity loaded with a** NV^- **like spin ensemble.** The black curve shows the transmission signal for the spin ensemble in $\langle S_z^2 \rangle = \frac{2}{3}$ state where the shift vanishes. The red and orange curves indicate the transmission signals for in $\langle S_z^2 \rangle = 0$ polarized ensembles with detuning of opposite sign. Due to the dependence on $(2\gamma_{||} + \gamma_\perp)$, the linewidth is broadened and the amplitude decreases. The parameters for plotting were chosen arbitrary but have reasonable magnitudes.

However, in dispersive regime, where the cavity is far detuned to the spin transition frequency, we can set $\Delta_s \approx \Delta$ because the probe field scanning range is around ω_c and orders of magnitude smaller than the detuning. Also, $\gamma_{||}$ and $\gamma_\perp$ are much smaller than Δ and they can be neglected. These estimations give the expression:

$$\langle a^\dagger a \rangle = \frac{\eta^2}{\kappa^2 + \left(\Delta_c + \frac{g_{eff}^2}{\Delta}(2 - 3\langle S_z^2 \rangle) \right)^2} \tag{4.55}$$

For our purpose, we are interested into the states of spin polarization with maximal and minimal shifts. The maximal shift emerges for $T \to 0$ where $\langle S_z^2 \rangle = 0$. For $T \gg \hbar\omega_s$, the spin polarization becomes $\langle S_z^2 \rangle = \frac{2}{3}$ and the dispersive shift vanishes.

26

$$\langle a^{\dagger} a \rangle_{ground} = \frac{\eta^2}{\kappa^2 + \left(\Delta_c + \frac{2g_{eff}^2}{\Delta} \right)^2} \tag{4.56}$$

Is the spin ensemble in its ground state, the resonance shift reaches its maximum value of $\frac{2g_{eff}^2}{\Delta}$. It should be mentioned that the direction of the shift is dependent of the detuning. When $\omega_s > \omega_c$ the shift is positive and for $\omega_s < \omega_c$ the shift is negative.

In thermal equilibrium for $T \gg \hbar\omega_s$, the shift component in the Lorentzian vanishes, the ensemble becomes transparent and (Eq. 4.55) transforms to the Lorentzian of the empty cavity, given by

$$\langle a^{\dagger} a \rangle_{therm} = \frac{\eta^2}{\kappa^2 + \Delta_c^2}. \tag{4.57}$$

To conclude, we specify a general expression for the dispersive cavity shift mediated by an NV^--like spin ensemble:

$$\chi = \frac{Ng_0^2}{\Delta} \left(2 - 3\langle S_z^2 \rangle \right) \tag{4.58}$$

In accordance with the Tavis-Cummings model in dispersive regime, the coupling strength g_0 of a single spin is enhanced by $\sqrt{N}$ and the shift is indirectly dependent on the detuning Δ.

Chapter 5

Spin-Phonon Relaxation Processes

This chapter provides an overview of processes which mediate spin-phonon relaxation of NV^- spins in diamond. Thermal excitations of the crystal lattice can be described as quasi-particles called phonons. These phonons generate spatial fluctuations of the crystalline magnetic and electric fields which, in turn, affect the wavefunction of local spin systems and can even induce spin flips.

In the thirties of the 20th century, the first efforts for the theoretical description of such spin-phonon relaxation were made [42, 43]. The models of Kronig [44] and Van Vleck [45] were able to match experimental data [46] for the first time. For low temperatures ($T < 4\,\mathrm{K}$), a sufficient model was developed by Elliot [47], Orbach [48] and Scott & Jeffries [49].

We want to depict a system consisting of an ensemble of N spins embedded in a phonon bath of constant temperature (Fig. 5.1). The spin has three levels, where only the ground state $|a\rangle$ and first excited state $|b\rangle$ are thermally populated. The second excited states ($|c\rangle$) eigenenergy is far above the energy of $|b\rangle$ and its thermal occupation is effectively zero. But its implementation is essential for the modelling of multi phonon processes.

For the description of the phonon bath, we apply the well known Debye model [50]. Within the Debye model, a phonon is seen as quantized collective crystal lattice
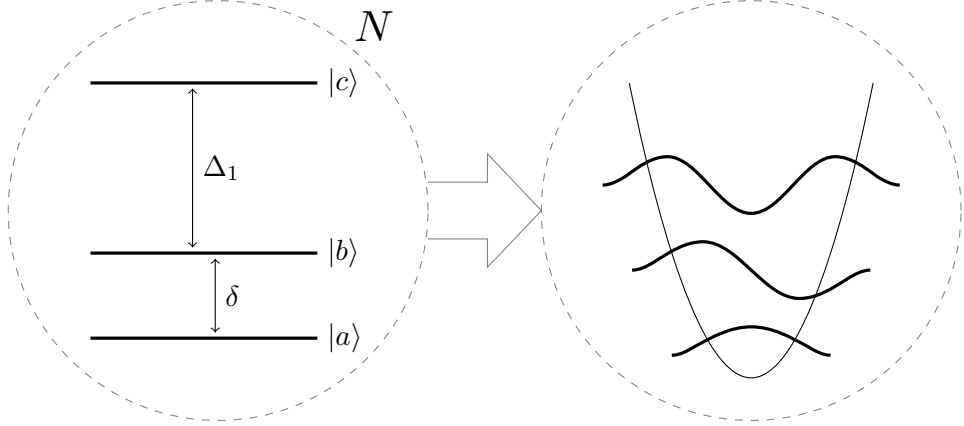
Figure 5.1: **Schematics of a spin ensemble relaxing into the phonon bath.** At the left hand side, the level structure of the spin system is shown. The second excited state $|c\rangle$ is introduced for the description of higher order spin-phonon decays. Furthermore, it is estimated that $\Delta_1 \gg \delta$ and $|c\rangle$ is not thermally populated. The right hand side illustrates the phonon structure of the Debye model. For the energy scales of our interest, the phonon structure becomes continuous.

excitation with an excitation number ruled by the Bose-Einstein statistics:

$$\bar{p}_0(\delta) = \frac{1}{exp(\frac{\delta}{k_B T}) - 1} \tag{5.1}$$

Here, $\bar{p}_0(\delta)$ is the excitation number of phonons with energy δ in thermal equilibrium, k_B is the Boltzmann constant and T the temperature.

Furthermore, the number of phononic modes in the crystal within a certain energy range $d\delta$ is given by:

$$\rho(\delta)d\delta = \frac{3V\delta^2}{2\pi^2\hbar^3 v^3}d\delta \tag{5.2}$$

It is a classical physical quantity and is dependent of the crystal volume V and of the material specific speed of sound v.

To conclude, we determine an equation of motion which can be applied universally for all spin-lattice relaxation processes to calculate the process specific relaxation rate $\gamma_i = \gamma_{\parallel,i} = T_{1,i}^{-1}$. We define the population inversion $n = N_a - N_b$, where N_a, N_b are the level population numbers and make a general ansatz for the equation of motion where

n relaxes into the state of thermal equilibrium with the population inversion n_0:

$$\dot{n} = -\gamma_{1,i}(n - n_0) \tag{5.3}$$

5.1 The Direct Process

Direct spin-phonon interaction means, that a two-level system emits or absorbs a single phonon. The phonon energy, corresponds to the transition energy δ of the two level system.

For the evaluation of the relaxation rate, we assume an ensemble of $N = N_a + N_b$ two-level systems in thermal equilibrium. The distribution of particles in ground and excited state is given by the Boltzmann distribution:

$$\frac{N_b}{N_a} = e^{-\frac{\delta}{k_B T}} \tag{5.4}$$

Similar to the emission and absorption of light by atoms, we can write the probabilities for spin flips induced by phonon emission and absorption:

$$P_{b \to a} = B_{b \to a}\big(\bar{p}_0(\delta) + 1\big) \tag{5.5}$$

$$P_{a \to b} = B_{b \to a}\bar{p}_0(\delta) \tag{5.6}$$

Note that there are two typs of phonon emission, stimulated emission induced by the presence of other phonons with energy δ and spontaneous emission. While the excited state is not degenerated, we can assume $B_{ab} = B_{ba} = B$, where B is a system dependent but temperature independent factor.

Now, we can use these probabilities to determine the rate equation for the level population numbers, given by

$$\dot{N_a} = -\dot{N_b} = N_b P_{b \to a} - N_a P_{a \to b} = B\big(N_b(\bar{p}_0(\delta) + 1) - N_a\bar{p}_0(\delta)\big). \tag{5.7}$$

Furthermore, we can apply this equation into (Eq. 5.3) and with the population inversion in thermal equilibrium

$$n_0 = N \tanh \frac{\delta}{2k_B T}, \tag{5.8}$$

we get the equation of motion which includes the relaxation rate of the direct process.

By solving (Eq. 5.3), a general expression for the relaxation rate is obtained:

$$\gamma_D = B \coth \frac{\delta}{2k_B T} \tag{5.9}$$

However, when the system is in the regime of $\delta \ll 2k_BT$, we can apply the series expansion of $\coth(\frac{\delta}{2k_BT})$ and get

$$\gamma_D \approx \frac{2Bk_B}{\delta}T. \tag{5.10}$$

It should be emphasized that if the direct spin phonon process is dominant, the relaxation rate becomes linear dependent on the temperature.

5.2 The Orbach Process

To explain the Orbach process we have to consider a three level system. We assume that the $|a\rangle \leftrightarrow |b\rangle$ transitions do not occur directly but can be mediated via the transition to the second excited state $|c\rangle$. First, the spin system in state $|a\rangle$ or $|b\rangle$ has to absorb a phonon to get into state $|c\rangle$. Afterwards, $|c\rangle$ decays into either $|a\rangle$ or $|b\rangle$ by emitting a phonon. Hence, the Orbach process is a two phonon process.

Like for the two-level system, the phonon emission and absorption probabilities for the three-level system are given by

$$P_{c\rightarrow a} = C_1\big(\bar{p}_0(\Delta_1 + \delta) + 1\big) \qquad\qquad P_{a\rightarrow c} = C_1\bar{p}_0(\Delta_1 + \delta), \tag{5.11}$$

for the $|a\rangle \leftrightarrow |c\rangle$ transitions and

$$P_{c\rightarrow b} = C_2\big(\bar{p}_0(\Delta_1) + 1\big) \qquad\qquad P_{b\rightarrow c} = C_2\bar{p}_0(\Delta_1), \tag{5.12}$$

for the $|b\rangle \leftrightarrow |c\rangle$ transitions. Its important to mention that this process only occurs when Δ_1 is less than the maximum phonon energy $k_B\Theta$, where Θ is the Debye temperature.

Now, we assume $\Delta_1 \gg \delta$ and we can consider $C_1 \approx C_2 \approx C$ to find the rate equations:

$$\dot{N}_a = C\big(N_c(\bar{p}_0(\Delta_1 + \delta) + 1) - N_a\bar{p}_0(\Delta_1 + \delta)\big) \tag{5.13}$$

$$\dot{N}_b = C\big(N_c(\bar{p}_0(\Delta_1) + 1) - N_b\bar{p}_0(\Delta_1)\big) \tag{5.14}$$

In a regime, where $k_BT \ll \Delta_1$, the population number of $|c\rangle$, N_c can be neglected. Furthermore, the assumption $\Delta_1 \gg \delta$ yield $\bar{p}_0(\Delta_1 + \delta) \approx \bar{p}_0(\Delta_1)$ and the rate equations are reduced to:

$$\dot{N}_{a,b} = -N_{a,b}\bar{p}_0(\Delta_1) \tag{5.15}$$

We insert these rate equations into Eq. 5.3, which gives an expression for the relaxation rate:

$$\gamma_O = C\bar{p}_0(\Delta_1) \approx C e^{-\frac{\Delta_1}{k_B T}} \tag{5.16}$$

If the Orbach process is dominant, the relaxation rate increases and saturates with increasing temperature.

5.3 The Raman Process

If a spin flip is induced by a simultaneous absorption of a phonon with energy δ_1 and an emission of a phonon with energy $\delta_2 = \delta_1 + \delta$, this process is called Raman process. In distinction to the Orbach process, the spin flip occurs via a virtual phonon state instead of a second excited state of the spin system.

The transition via an virtual phonon modifies the transition probabilities compared to the previously discussed probabilities. The simultaneous absorption and emission is modelled by the product of the probabilities for each process.

$$P_{a \to b} = D\bar{p}_0(\delta_2)\big(\bar{p}_0(\delta_1) + 1\big) \qquad P_{b \to a} = D\bar{p}_0(\delta_1)\big(\bar{p}_0(\delta_2) + 1\big) \tag{5.17}$$

Again, we use these probabilities to construct Eq. 5.3 for the Raman process. Though, we have to consider the continuity of the phonon spectrum. To do so, we have to integrate over all possible virtual phonon states and, therefore, all possible decay channels. Hence, we can write the rate equation:

$$\dot{N}_b = D' \int \Big[N_a \bar{p}_0(\delta_2)\big(\bar{p}_0(\delta_1) + 1\big) - N_b \bar{p}_0(\delta_1)\big(\bar{p}_0(\delta_2) + 1\big) \Big] \delta_1^6 \, \mathrm{d}\delta_1 \tag{5.18}$$

Depending on temperature and spin structure, there are several solutions for the Raman-induced relaxation [51]. We restrict ourself to two regimes:

- $\delta_1 \ll \delta$ and $\delta \gg k_B T$:

  The exponential functions in the probabilities can be written as Taylor series which yields the temperature dependence of the relaxation rate:

  $$\gamma_R \propto T^4 \tag{5.19}$$

- $\delta_1 \gg \delta$ and $\delta \ll k_B \Theta$:

  In this regime, the integration in Eq. 5.18 leads to a temperature dependence of the relaxation rate:

  $$\gamma_R \propto T^7 \tag{5.20}$$

5.4 The Phonon Bottleneck

For the description of the previously discussed relaxation processes, we assumed that the spins decay into phononic modes in thermal equilibrium. However, in the experiment, the phononic system has to be coupled to an external heat bath to conserve the phonon population [49, 52]. If the phonon-bath coupling is weaker than the spin-phonon coupling, the phonon temperature is greater than the bath temperature and a phonon bottleneck occurs.

The total rate equation for the phonon excitation number is

$$\frac{\mathrm{d}\bar{p}}{\mathrm{d}t} = \frac{1}{2}\frac{\dot{n}}{\Delta\delta\ \rho(\delta)} - \tau_{bath}(\bar{p} - \bar{p}_0). \tag{5.21}$$

The first term represents the phonon alteration per spin variation, where $\Delta\delta$ is the bandwidth of the spins interacting with phonons and the second term describes the phonon decay into the heat bath with rate τ_{bath}. A bottleneck only occurs when the right hand side of (Eq. 5.21) is greater than zero.

Next, we have to consider τ_{bath} determining processes. In general, we can distinguish two separate classes of phonon-bath relaxation processes.

Spatial relaxation means a spatial transport of the excitation into the bath, the phonon is transmitted into the bath directly. The relaxation rate $\tau_{bath} \approx \frac{v_s}{l}$ is determined by the speed of sound within the lattice, v_s and the diameter of the crystal, l. A bottleneck occurs when v_s is slow compared to the spin relaxation rate or when l is large and, therefore, the spatial transport into the bath is also too slow.

The second class are spectral relaxation processes. These processes scatter phonons inelastically and reduce the excitation number $\bar{p}_0(\delta)$ of the phonon bands, which exchange excitations with the spin system. Examples for such processes are inelastic scattering at the crystal surface, phonon-phonon collisions and scattering by lattice-defects or impurities.

As we can see in the first term of (Eq. 5.21), also the present spin-phonon relaxation process determines the occurrence of the bottleneck. Since we want to consider a system where $\delta < k_B T \ll k_B \Theta$, we can neglect the Raman process as cause for a bottleneck. Due to the wide bandwidth ($\Delta\delta$) and high energy of the involved phonons, where $\bar{p}_0$ is small, the term of the spin-phonon relaxation becomes small compared to the phonon-bath relaxation term in (Eq. 5.21).

In this regime, also the Orbach process is negligible. We assumed that $\Delta_1 \gg \delta$

and, therefore, the excitation numbers of the involved phonons, $\bar{p}_0(\Delta_1)$ and $\bar{p}_0(\Delta_1 + \delta)$ become small again. The first term in (Eq. 5.21) becomes small as well and a bottleneck can not occur.

At last, we discuss the direct spin-phonon relaxation in terms of a bottleneck. The direct process is mediated by absorption and emission of a single phonon, which has a energy equal to the spin transition energy. When $\delta < k_B T$, the thermal excitation of these phonons can not be neglected and a bottleneck can occur. To determine the temperature dependence of this bottleneck, we have to consider the real relaxation that we are measuring in experiment. We are not able to measure the spin-phonon and phonon-bath relaxation separately, instead we measure the total spin-bath relaxation. Its rate can be approximately written as

$$\gamma_{tot} = \frac{\gamma_D \, \gamma_1}{\gamma_D + \gamma_1}, \tag{5.22}$$

where $\gamma_D \approx AT$, is the spin-phonon relaxation rate and γ_1 is the real spin-bath relaxation rate. Note that $\gamma_1 \neq \gamma_{bath}$ because it is also dependent on the phonon-band energy (E_{ph}) and on the Zeeman energy of the spin ensemble (E_s). Therefore, γ_1 is given by

$$\gamma_1 = \gamma_{bath} \frac{E_{ph}}{E_s} \approx DT^2, \tag{5.23}$$

for the low spin-transition energy and low temperature regime.

If we put these results for the particular rates into (Eq. 5.22), we find that the measured relaxation rate γ_{tot} becomes proportional to T^2 for a dominant bottleneck ($\gamma_1 \gg \gamma_D$):

$$\gamma_{tot} = \frac{ADT^3}{AT + DT^2} \approx DT^2 \tag{5.24}$$

To summarize all previously discussed spin-phonon respectively spin-bath relaxation processes, each process has a relaxation rate with distinct temperature dependence. Hence, this temperature dependence allows to study and distinguish every single process in experiment.

5.5 Considerations for the NV^- system

We are interested into spin-phonon interaction of the $^3A_2$ triplet state in a temperature range of 35-300 mK. In this regime, the phononic modes with energy corresponding to

the spin transition energy δ are weakly populated. Therefore, the probability for double phonon processes becomes negligible and only the direct process can occur.

Since the NV^- has a degenerate excited state we have to modify the rate equations of the direct process. The probabilities for the $|m_s = 0\rangle \leftrightarrow |m_s = +1\rangle$ and $|m_s = 0\rangle \leftrightarrow |m_s = -1\rangle$ transitions are given by (Eq. 5.5) and (Eq. 5.6) and we can write the rate equations for the level population numbers as

$$\dot{N}_0 = N_{+1}P_{+1\to0} + N_{-1}P_{-1\to0} - N_0 P_{0\to+1} - N_0 P_{0\to-1} \tag{5.25}$$

and

$$\dot{N}_{\pm1} = N_0 P_{0\to\pm1} - N_{\pm1}P_{\pm1\to0}. \tag{5.26}$$

The degeneracy yields $N_{+1} = N_{-1} = N_{\pm1}$ and the rate equations transform to

$$\dot{N}_0 = 2B\big(N_{\pm1}\big(\bar{p}_0(\delta) + 1\big) - N_0\bar{p}_0(\delta)\big) \tag{5.27}$$

and

$$\dot{N}_{\pm1} = -B\big(N_{\pm}\big(\bar{p}_0(\delta) + 1\big) - N_0\bar{p}_0(\delta)\big). \tag{5.28}$$

Furthermore, we have to redefine the population inversion as $n = N_0 - 2N_{\pm1}$ with an expression for the thermal equilibrium given by

$$n_0 = N\left(1 - \frac{2}{\exp(\frac{\delta}{k_B T}) + 2}\right). \tag{5.29}$$

Next, we apply the new defined population inversion and the rate equations into (Eq. 5.3) to obtain an expression for the relaxation rate:

$$\Gamma(T) = \Gamma_0\big(1 + 3\bar{p}_0(\delta, T)\big) \tag{5.30}$$

Compared to the relaxation rate of the direct process for the two level system, the relaxation rate for the NV^- has a similar temperature dependence. For $T \gg \delta$, the direct process is linear dependent to T. In a regime where $T \ll \delta$, the phonon population $\bar{p}_0(\delta)$ becomes negligible and the process is dominated by spontaneous emission.

Chapter 6

Experimental Set-up

In the previous chapters, we discussed diamond as spin ensemble host, microwave cavities and the theoretical background of spin-cavity interaction. The following part of this thesis introduces the experimental set-up required for the measurement of the longitudinal relaxation of a NV^- ensemble at cryogenic temperatures. First, we discuss the operational mode of a pulse-tube driven adiabatic demagnetization refrigerator (ADR), which enables to cool down and stabilize at temperatures in a range of $50\,$mK-$1\,$K. Afterwards, the set-up of the microwave transition spectroscopy is explained.

6.1 Pulse-Tube driven ADR Cryostat

In our laboratory, the cryostat 'Model 103 Rainier' from High Precision Devices, Inc. is installed. The refrigerator itself consists of two distinct cooling units. The two-stage pulse tube cryocooler 'PT 407 RM' from Cryomech, Inc. provides cooling for the $50\,$K and $3\,$K stage. At the $3\,$K stage, the ADR itself is installed.

To prevent heat transfer and condensation and freezing of ambient gases, the cryostat is evacuated, to a pressure of $p \leq 3 \cdot 10^{-5}$mbar. Another measure to prevent radiative heating is the installation of the $50\,$K and $3\,$K shields, which insulate stages with lower temperatures. Fig. 6.1 shows a section view of the cryostat.

6.1.1 Pulse Tube Refrigerator

The purpose of the pulse tube refrigerator (PT) is to pre-cool the experiment to reduce the heat load of the ADR and to transfer the heat which is dissipated during the ramping
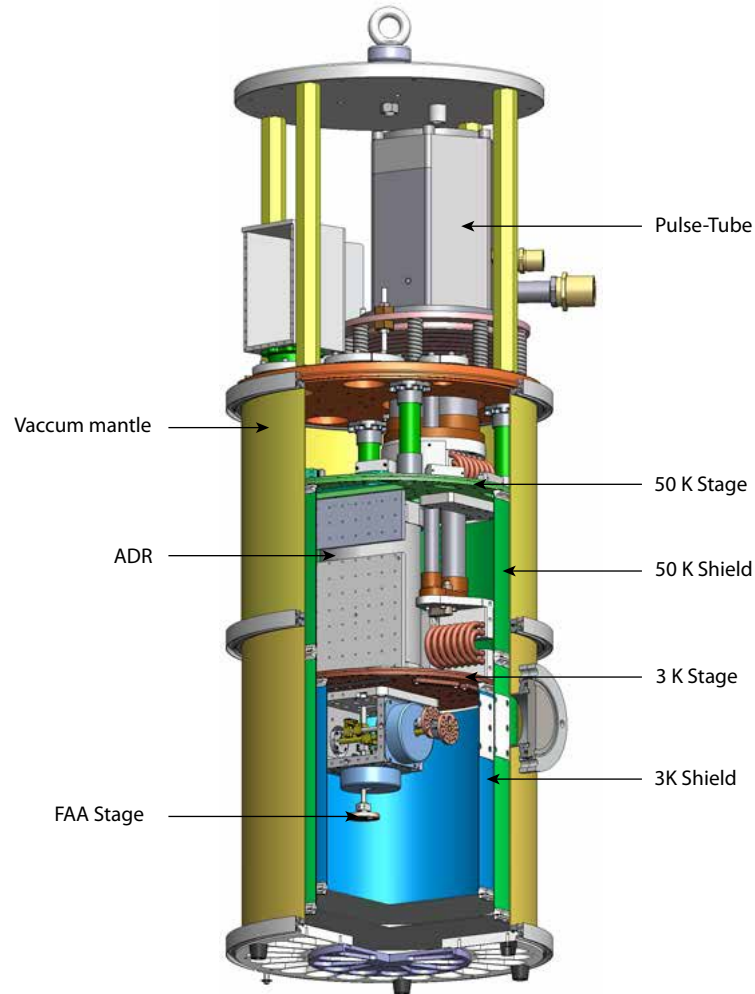
Figure 6.1: **Section view of the Cryostat.** (Picture taken from High Precision Devices, Inc. [53])

of the ADR magnet. Within this thesis, only the basic functional principle of a PT, which was presented by Gifford & Longsworth in 1964 [54] will be discussed. For information on more advanced concepts of PTs [55, 56, 57] is recommended.

The cooling by a PT is based on the effect, that a flow of a gas with constant temperature into a volume V, leads to an increase or decrease of pressure dependent on the direction of the flow. Hence, the inner energy of the gas varies by the caloric energy

$$Q = V\Delta p, \tag{6.1}$$

where Δp is the variation of pressure. When we consider a small volume element with

a gas flow entering from the left, the release of the caloric energy leads to an increase of temperature at the right hand side of the volume element. A temperature gradient within the volume element builds up. In the case of gas streaming out of the volume element at the left side, Q becomes negative and the temperature at the left side increases.
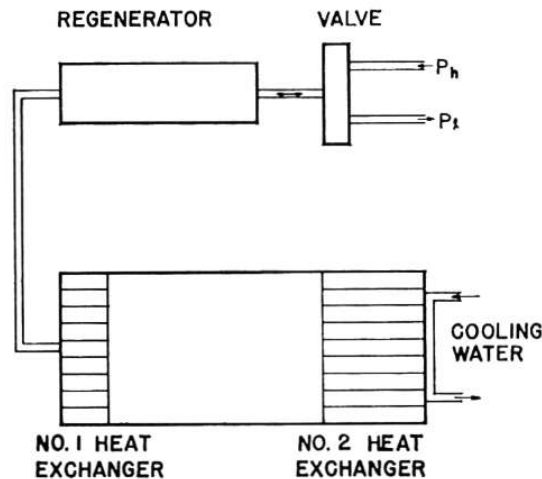
Figure 6.2: **Schematic of a basic pulse tube refrigerator.** (Figure taken from [54])

A PT utilizes this heat transport for cooling. To illustrate its operating mode, we discuss a complete cooling cycle based on Fig. 6.2. At the beginning, the rotary valve opens the high pressure line and gas flows into the cylindric volume between the two heat exchanger. The temperature at the right hand side increases. Yet, the water cooling keeps the second heat exchanger at a constant temperature and transfers the caloric energy. Next, the rotary valve switches to the low pressure line, consequently the direction of the gas flow gets reversed and the first heat exchanger gets cooled. The rotary valve switches again to the high pressure line and the next cycle starts. Due to the regenerator, the entering gas gets cooled and does not heat up the first heat exchanger.

In our experimental set up, the two stage pulse tube cryostat 'PT 407 RM' from Cryomech, Inc. is installed. Two helium driven pulse tubes in series cool the 50 K and 3 K stage. In operational mode, the high pressure line is pressurized with $\sim 21.5 - 22$ bar and the low pressure line width $\sim 7.5 - 8$ bar. The pressure fluctuation is caused by the additional pulse tube volume while switching.

6.1.2 ADR -Adiabatic Demagnetization Refrigerator

Magnetocaloric effect

The alternation of the temperature of magnetic materials in dependence of the variation of the applied magnetic field is called magnetocaloric effect. Warburg [58] observed this effect for the first time in 1881. A theoretical description of the magnetocaloric effect and the suggestion of its application in refrigerators was given by Debye [59] and Giauque [60]. Since then, ADRs became an important tool for science as they enable to reach a temperature regime of a few µK. Even commercial applications are in development since ADRs are more energy efficient than classical gas compression refrigerators. The given description of the magnetocaloric effect follows the review of Pecharsky & Gscheidner [61], which is also recommended for further information.

The origin of this effect is the alteration of the magnetic entropy S_M of magnetic or paramagnetic materials in dependence on temperature and external magnetic fields. The entropy S of a material at constant pressure is given by

$$S(T, H) = S_M(T, H) + S_{Lat}(T, H) + S_{El}(T, H), \qquad (6.2)$$

where S_{Lat} is the lattice entropy and S_{El} is the electronic entropy which can be neglected in the present consideration. In consequence of the constant entropy of the material, the variation of the magnetic entropy S_M causes a response of the lattice entropy S_{Lat} and vice versa. When the magnetic moments get polarized, S_M rises and S_{Lat} has to decrease. Therefore, the lattice temperature has to rises. Nevertheless, when S_M and the polarization of the magnetic moments shrinks, S_{Lat} rises and we can observe a cooling effect.

To find an theoretical description of the magnetocaloric effect, we have to consider that T and S_M are correlated with the magnetization and the external magnetic field. We make use of Maxwell's relations

$$\left(\frac{\partial S(T, H)}{\partial H}\right)_T = \left(\frac{\partial M(T, H)}{\partial T}\right)_H \qquad (6.3)$$

and integrate the right hand side over the alteration of the external magnetic field H to get an expression for the variation of the magnetic entropy:

$$\Delta S_M(T, \Delta H) = \int_{H_1}^{H_2} \left(\frac{\partial M(T, H)}{\partial T}\right)_H \mathrm{d}H \qquad (6.4)$$

Hence, we can see that an increase of H enhances S_M and vice versa. From the relation $C\mathrm{d}T = -T\mathrm{d}S$ where C is the materials heat capacity, we are able to transform Eq. 6.4 to

$$\Delta T\left(T, \Delta H\right) = -\int_{H_1}^{H_2} \left(\frac{T}{C(T,H)}\right)\left(\frac{\partial M(T,H)}{\partial T}\right)_H \mathrm{d}H.　\qquad (6.5)$$

Again, the negative sign of this equation elucidates the indirect proportionality between ΔS_M and ΔT.

For the purpose of cooling devices, paramagnetic materials are used because their heat capacity is very small, which increases ΔT. To generate adiabatic cooling, the external field orientates the magnetic moments of the paramagnet. When the field is ramped down, the magnetic moments randomize and cooling occurs.

Set-up of the ADR

In our set-up, the ADR is installed at the $3\,\mathrm{K}$ stage. Its core consists of two paramagnetic salts. The Gadolinium Gallium garnets (GGG) purpose is to precool and reduce the heat load for the second salt. Furthermore, the Ferric Ammonium Alum (FAA) enables to cool down to a few tens of mK. Dependent on the heat load at the FAA stage, temperatures below $50\,\mathrm{mK}$ can be reached temporarily.

These salts are enclosed by a superconducting coil which can be loaded with a current of up to $9.2\,\mathrm{A}$. The current and, therefore, the applied magnetic field can be controlled, which enables temperature stabilization. Depending on the heat load, the FAA stage can be stabilized at $50\,\mathrm{mK}$ for approximately $16\,\mathrm{h}$. For higher temperatures the time at which the temperature is stable increases massively.

To prevent distortions due to external magnetic fields and heat flow from the $3\,\mathrm{K}$ stage, the paramagnetic salts and the coil are enclosed by a cylindric mu-metal shield.

6.1.3　Demagnetization Cycle

An important characteristic of ADRs is that they can not provide continuous cooling. As soon the external magnetic field is ramped down completely, magnetization of the paramagnetic salt reaches its minimum and no further cooling is possible. In order to restart cooling, the external magnetic field and the magnetization of the paramagnetic salt has to be reset. Therefore, the ADR can only cool in a cyclic mode.

Such a typical demagnetization cycle of the refrigerator used in this experiment is shown in Fig. 6.3. When the FAA stage reaches $3\,\mathrm{K}$ at the first cooldown or a new
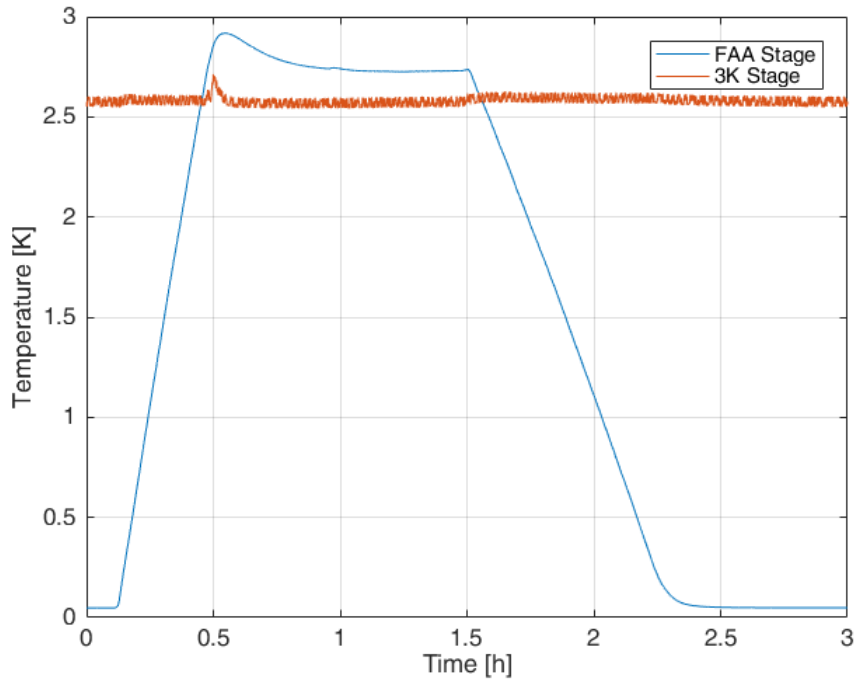
Figure 6.3: **Temperature progression during a complete cooldown.** At the start of the cooling cycle the magnet is ramped up and the temperature of the FAA stage increases. Next, the heat switch closes and the soak time starts. In the diagram, the heat switch closes at 0.5 h, the FAA stage is cooled and the temperature of the 3 K stage increases briefly. For this cycle a soak time of 1 h was chosen. Afterwards, the heat switch opens again and adiabatic cooling of the FAA stage starts.

demagnetization cycle is started, ramping up of the coil current starts. The increase of the magnetic field generates heating of the paramagnetic salts. Thus, the heat switch is closed and the heat is transferred to the pulse tube cooled 3 K stage. The manually adjustable time to get rid of the thermal discharge, where the FAA stage is connected with the 3 K stage is called 'soak time'. For our set-up a soak time of one to two hours is reasonable.

After this time, the heat switch is open and the coil current is ramped down and the magnetocaloric effect cools the FAA stage. For temperature stabilization, the coil current is PID controlled.

6.2   Microwave Spectroscopy

Since we want to measure the dispersive shift of a microwave cavity induced by longitudinal relaxation of a NV^- ensemble in diamond, we have to build a microwave spectroscopy set-up. In general spectroscopy is a well known and powerful tool of physics with a wide range of applications.
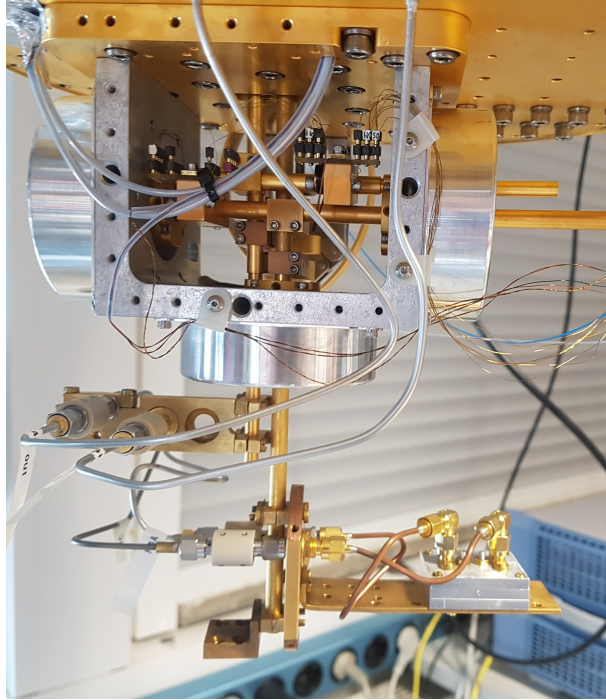
Figure 6.4: **Picture of the FAA stage with mounted Al cavity.**

Microwave spectroscopy has an advantage towards e.g. optical spectroscopy, since microwave components are robust and well developed due to their utilization in commercial telecommunication networks.

The vector network analyzer (VNA) ZNB8 from Rhode & Schwarz is used for transmission spectroscopy. It is capable to provide continuous coherent microwave signals from $9\,\text{kHz}$ to $8.5\,\text{GHz}$. For transmission spectroscopy, the VNA displays $|S_{21}|^2$, where scattering parameter $S_{21} = V_2^+/V_1^-$ is defined as ratio between the incident signal amplitude at port 2 (V_2^+) and the outgoing signal amplitude at port 1 (V_1^-).

In order to prevent saturation of the spins, the cavity is probed with an input power of $-110\,\text{dBm}$ which corresponds to an average number of 1×10^{-9} photons per spin in

the cavity.

In order to measure at room temperature, the cavity transition signal is amplified twice. At the 3 K stage the amplifier LNC 4-8A from Low Noise Factory for cryogenic environment with a gain of $+39$ dB is integrated in the up-line. The ultra low noise amplifier form MITEQ has a gain $+30$ dB and is installed at room temperature. To prevent heat conduction via the coaxial cables, DC blocks and attenuators with -60 dB are implemented into the up- and down-line between the FAA, 1 K and 3 K stage.

In Fig. 6.5 the schematic spectroscopy set-up and its thermal segmentation is shown.
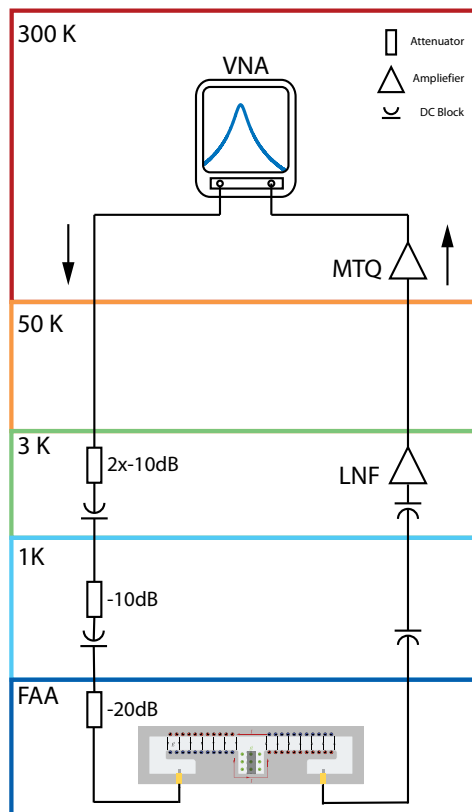
Figure 6.5: **Schematics of the spectroscopic set-up.** The VNA probes the 3D cavity with the diamond. DC blocks and attenuators in the down- and up-line prevent heat conduction. Two amplifier are integrated in the up-line. Note that the room temperature amplifier was not used for all measurements.

Chapter 7

Measurements and Data Analysis

Previously, we presented the theoretical concepts and properties of NV^- center in diamond as solid state spin ensemble in a 3D microwave cavity. Furthermore, we discussed spin-phonon relaxation processes and the experimental set-up available in our laboratory.

The first part of this chapter presents the measurement method to observe longitudinal relaxation of a NV^- ensemble in a temperature range of $25 - 300 \,\mathrm{mK}$. The presented experimental design, where the spin ensemble is dispersively coupled to the cavity enables us to measure the collective spin state indirectly. Hence, this method is distinguished from previous measurements [16, 62], which measured the longitudinal relaxation rate with a ODMR set-up down to a temperature of $4 \,\mathrm{K}$.

The second part introduces the properties of the measured diamond samples and properties of the used cavities and in the final part, measurements of the longitudinal relaxation rate Γ_1 are presented. Further on, the temperature dependence of Γ_1 and the fundamental process is discussed. It is shown that the ultimate limit of Γ_1 is the spontaneous emission into phononic vacuum modes. Finally, the achieved data and models are compared to a theoretical calculations of Johannes Gugler [63]. It shall be mentioned that the presented experiment, measured data and the comparison with the theoretical model are published in [21].

7.1 Measurement Sequence

For measurement, the diamond samples are bonded with vacuum grease in between the bow ties of a detuned cavity, where $\Delta = \omega_s - \omega_c \gg g_N$. In order to initialize the collective spin state, the spin ensemble is kept at $2.7\,\text{K}$ during the soak time of an ADR demagnetization cycle. At this temperature, the expectation value of the NV^- spin polarization is given by $\langle S_z^2 \rangle \approx \frac{2}{3}$ (see (Eq. 7.1) and Fig.7.2). Afterwards, we stabilize the system at temperatures between 60-300 mK. The bottom limit of the temperature is given by the ADR and the upper restriction is caused by the phase transition into the superconducting phase of the aluminium cavity. When the temperature is stabilized, the phonon population is well defined and we probe the transmission of the cavity with the VNA continuously to measure the spin polarization decay into the thermal equilibrium with the lattice, mediated by spin-phonon interaction. The spin polarization in thermal equilibrium is given by

$$\left\langle S_z^2(T)\right\rangle_{st} = \frac{2}{e^{\frac{\hbar\omega_s}{k_BT}} + 2}. \tag{7.1}$$

The longitudinal relaxation process can be described with the following differential equation:

$$\frac{\mathrm{d}}{\mathrm{d}t}\left\langle S_z^2(t,T)\right\rangle = -\Gamma_1\left(\left\langle S_z^2(t,T)\right\rangle - \left\langle S_z^2(T)\right\rangle_{st}\right), \tag{7.2}$$

here $\left\langle S_z^2(t,T)\right\rangle$ is the time dependent spin polarization and Γ_1 is the relaxation rate.

In Fig. 7.1 the thermal spin polarization for NV^- is shown. Because the magnetic-dipole transition $|m_s = 0\rangle \leftrightarrow |m_s = \pm 1\rangle$ corresponds to $138.2\,\text{mK}$, the spin polarization varies stronger below $0.4\,\text{K}$ compared to the spin polarization at higher temperatures. This temperature dependent variation of the spin polarization is the foundation of the measurement scheme which is presented here. The spin ensemble is initialized at a certain temperature, then the temperature is changed and the spin ensemble relaxes into thermal equilibrium via interaction with phonons.

The rate equation (Eq. 7.2) leads an exponential decay. Hence, Γ_1 is only dependent on the phonon population defined by the base temperature. The cooldown time of the ADR in the order of 20-40 min is fast enough for the measurement because the spin-phonon coupling is weak and it is a too short time for the spins to relax completely.

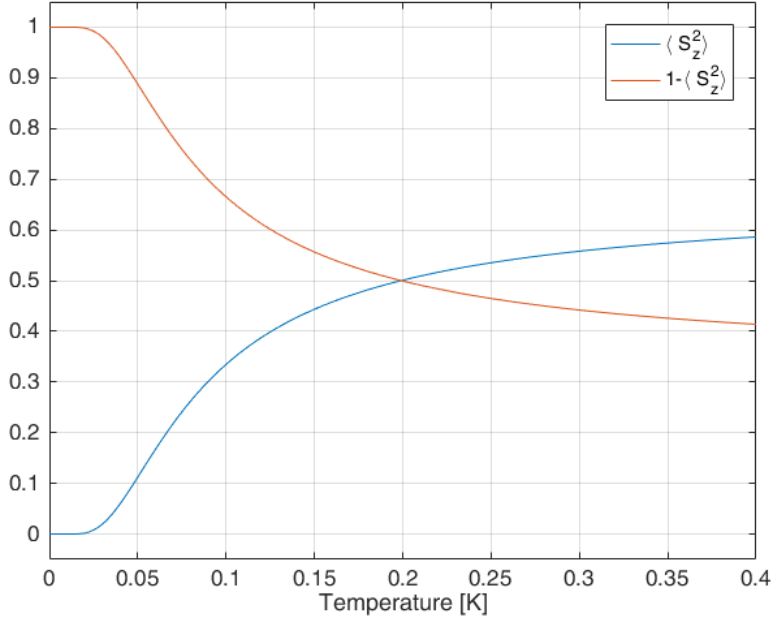As previously discussed (Sec. 4.5.2), the resonance frequency of the cavity experiences

Figure 7.1: **Spin polarization of** NV^- **below** $0.5\,\mathrm{K}$**.** The blue line illustrates the thermal spin polarization and the orange line illustrates the thermal population of the $|m_s = 0\rangle$ state.

a shift proportional to $\langle S_z^2(t,T)\rangle$ given by

$$\chi(t,T) = \frac{Ng_0^2}{\Delta}\left(2 - 3\left\langle S_z^2(t,T)\right\rangle\right) \tag{7.3}$$

and the shift observed in experiment given by

$$\Delta\chi(T,t) = \chi(T,t_0) - \chi(T,t), \tag{7.4}$$

where t_0 is the time of the first transmission spectrum taken.

An example of measured transmission spectra (traces) of such a relaxation process is given in Fig. 7.2. Because the cavity has an eigenfrequency above the spin transition, we observe a negative resonance shift for relaxation to lower temperatures. Also the broadening of the relaxed resonances corresponds to the description given in Sec. 4.5.2.
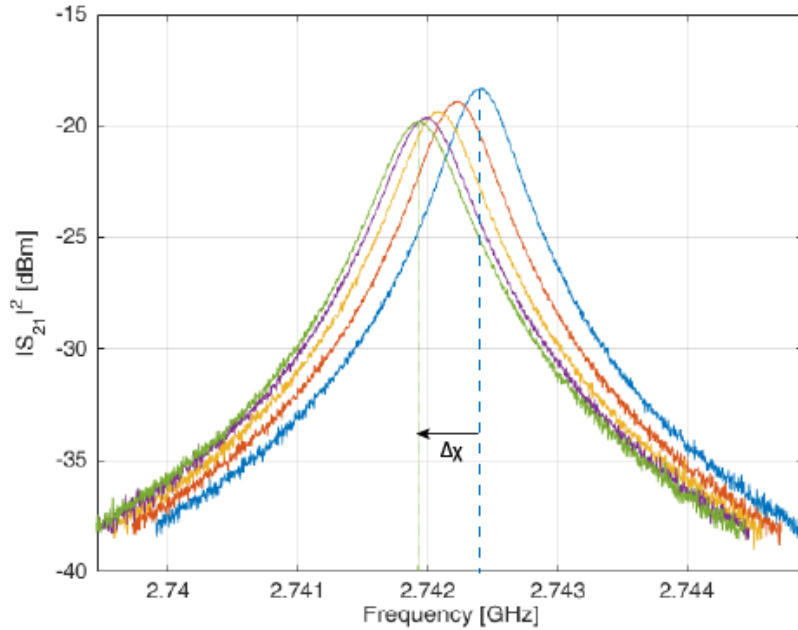
Figure 7.2: **Transmission spectra taken during the relaxation of the N1 sample at** $80\,\mathrm{mK}$**.** The sample was measured with the aluminium cavity with improved design.

7.2 Diamond samples

Beside a natural abundance of NV^- in diamond, we can create dense NV^- ensembles with neutron or electron irradiation of diamonds and annealing. The particle impact creates vacancies which pair with nitrogen impurities while annealing.

Four different diamond samples which differ in NV^- density and irradiation type were measured:

- **Neutron irradiated sample N1:**

  The commercially available type-Ib diamond, bought from Element Six Ltd. is a high-pressure, high-temperature (HPHT) diamond with initial nitrogen concentration of $< 200\,\mathrm{ppm}$ and natural abundance of ^{13}C. It was neutron irradiated at the TRIGA Mark II reactor of the TU Wien. The sample was irradiated in a energy range of 0.1-$2.5\,\mathrm{MeV}$ with a total dose of $9 \times 10^{17}\,\mathrm{cm}^{-2}$ for $50\,\mathrm{h}$ and afterwards annealed for $3\,\mathrm{h}$ at $900\,°\mathrm{C}$. The detailed sample preparation is given in [64] (sample

BS3-1b).

- **Electron irradiated samples E1 and E2:**

  Both samples are type-Ib HPHT diamonds with initial nitrogen concentration of 100 ppm and 50 ppm. The samples were irradiated with with 2 MeV electrons at 800 °C and annealed at 1000 °C several times at a Cockcroft-Walton accelerator of the QST, Takasaki. The E1 sample was irradiated with a total dose of $1.1 \times 10^{19} \, \mathrm{cm}^{-2}$ and has a NV^- density of 40 ppm. The E2 sample was irradiated with a total dose of $5.6 \times 10^{18} \, \mathrm{cm}^{-2}$ and has a NV^- density of 13 ppm.

- **Electron irradiated samples E3:**

  Like the N1 sample, the sample originates from Element Six Ltd., is a type-Ib HPHT diamond and has the same initial N and ^{13}C concentration. The sample was electron irradiated at the linear accelerator of the Instituto per la Sintesi Organica e la Fotoreattivita in Bologna, Italy with an electron energy of 6.5 MeV at 750-900 °C and a total dose of $1.0 \times 10^{18} \, \mathrm{cm}^{-2}$. Its NV^- density is 10 ppm. Detailed information about the sample preparation is given in [64] (sample U5).

Sample	N1	E1	E2	E3
NV^- [ppm]	40	40	13	10
NV [ppm]	< 200	100	50	< 200
Irradiation type	n	e^-	e^-	e^-
Irradiation energy [MeV]	0.1-2.5	2	2	6.5
Irradiation dose [cm^{-2}]	9.0×10^{17}	1.1×10^{19}	5.6×10^{18}	1.0×10^{18}
Mass [mg]	19.2	44.6	22.6	10.8

Table 7.1: **Comparison diamond sample properties.**

7.3 3D Aluminium cavity

We used two different 3D lumped element cavities machined out of aluminium (EN AW 6066) for the measurements. The data of the E1 sample was taken with the prototype cavity and the data of the other samples was measured with a new designed cavity with tunable bow tie distance and changeable frame. Compared to the new design, the prototype has a fixed bow tie distance, a more massive body and consists of only two aluminium parts. Pictures of both cavities can be found in App. A.
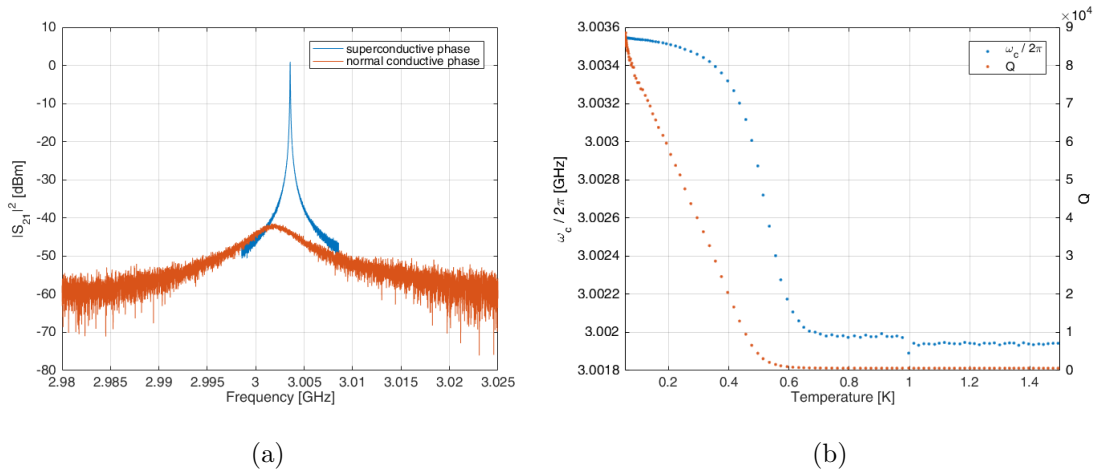

(a)   (b)

Figure 7.3: **Properties of the prototype cavity during cooldown.** (a) Transmission spectra of the superconducting cavity at $55\,\mathrm{mK}$ and of the normal conductive cavity at $2.93\,\mathrm{K}$. (b) Evolution of ω_c and Q during a full cooldown.

Aluminium was chosen as cavity material because it is a type 1 superconductor with a critical temperature of $T_c = 1.14\,\mathrm{K}$. In superconducting phase, the Q factor of the cavity is remarkably enhanced and we were able to show that these bow tie cavities can have Q factors of almost 1×10^5. This is advantageous, because the high Q cavities enables us to perform much more sensitive measurements of the dispersive shift due to the higher resolution of the resonance frequency ω_c. At the left panel of Fig. 7.3 we show the transmission signal of the the prototype cavity at $55\,\mathrm{mK}$ and $2.93\,\mathrm{K}$. Due to the superconducting phase transition the cavity reaches $Q = 8.8 \times 10^4$ compared to $Q \approx 600$ in normal conductive phase. The plot in the right panel shows the evolution of ω_c and Q of the prototype during a full cooldown. At $1\,\mathrm{K}$, the cavity starts to become superconductive, we observe a small step in ω_c. Afterwards, when the complete cavity

50

condensates into the superconducting phase, we observe a shift of ω_c of $2.4\,\mathrm{MHz}$. During this phase, also Q rises.

Furthermore, we compare the properties of the prototype cavity during cooldown and warm up (see Fig. 7.4). We can see that during warm up, ω_c and Q are constant until the starting phase transition at $0.3\,\mathrm{K}$. The observed difference of temperature dependence can be traced back to the cavity design. The prototype is machined out of a massive aluminium body. Therefore, it could be that the heat load at the FAA stage is larger and the real temperature of the cavity is higher than the temperature of the heat sensor during cooldown. Another origin for the difference of temperature dependence could be a design dependent phase transition time. During warm up, this is not an issue anymore and the measurements taken during warm up display the true temperature dependence of the prototype cavity.

(a)   (b)
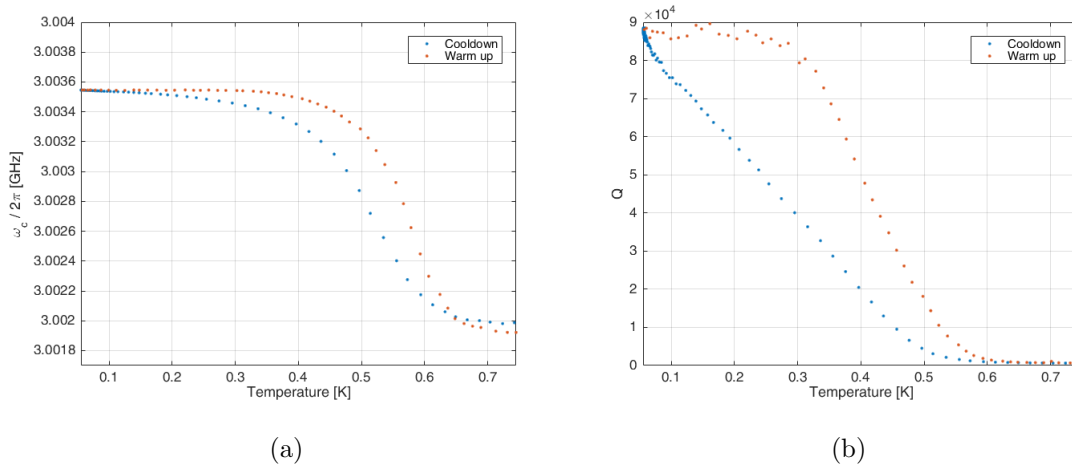
Figure 7.4: **Comparison of ω_c and Q of the prototype** during cooldown and warm up.

The observed shift of ω_c illustrated in Fig. 7.5 at stabilized temperatures displays the relaxation of the prototype cavity to the temperature of the FAA stage and corresponds to the difference of ω_c between cooldown and warm up. We also see that this relaxation decreases with lower temperature. However, this resonance frequency and Q relaxation of the empty cavity has to be considered for the measurement of the spin-phonon relaxation.
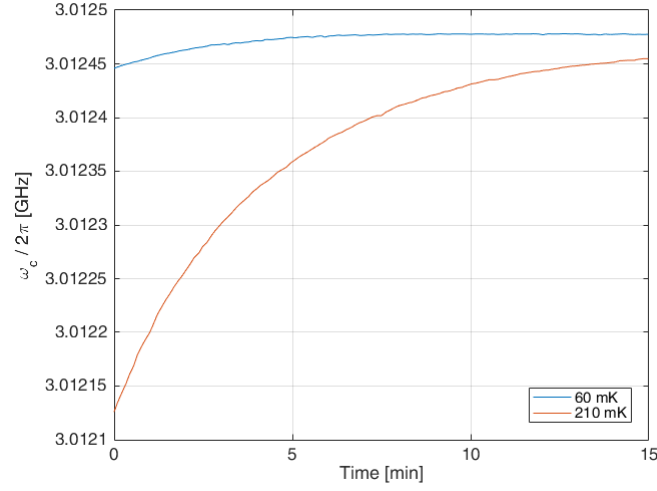
Figure 7.5: **Prototyp cavity relaxation** at stabilized FAA stage temperature.

(a)   (b)
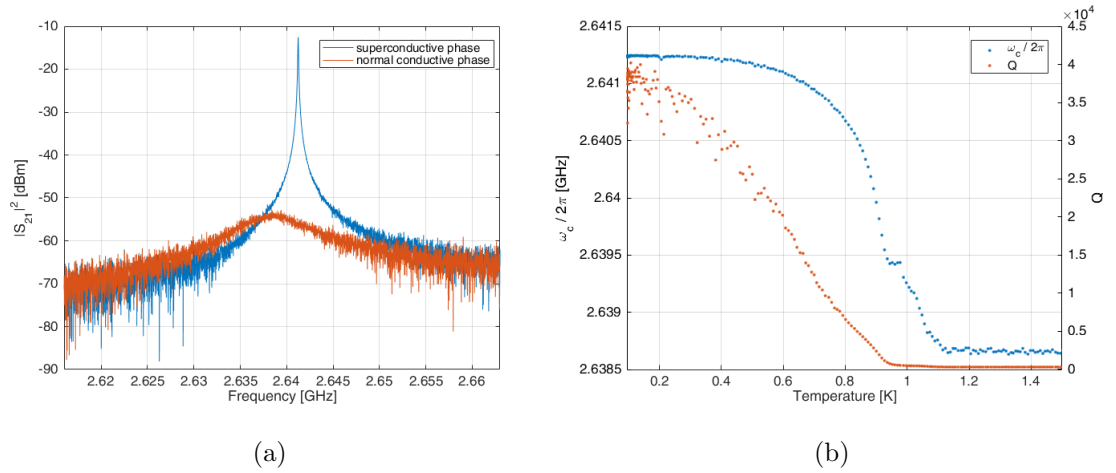
Figure 7.6: **Properties of the cavity with improved design during cooldown.** (a) Transmission spectra of the superconducting cavity at $96\,\mathrm{mK}$ and of the normal conductive cavity at $2.619\,\mathrm{K}$. (b) Evolution of ω_c and Q during a full cooldown. Compared to the prototype the cavity becomes superconducting at higher temperatures. The broad distribution of Q is caused by distortions of unknown origin.

Compared to the prototype, the cavity with new design has improved properties. Due to the down-scaled body, the transition to the superconducting phase happens at

higher temperatures (see Fig. 7.6a) and we can not observe any different temperature dependence of ω_c during cooldown and warm up (see Fig. 7.7a). Therefore, the resonance frequency relaxation of the empty cavity at stabilized temperature is small and can be neglected.

(a)   (b)
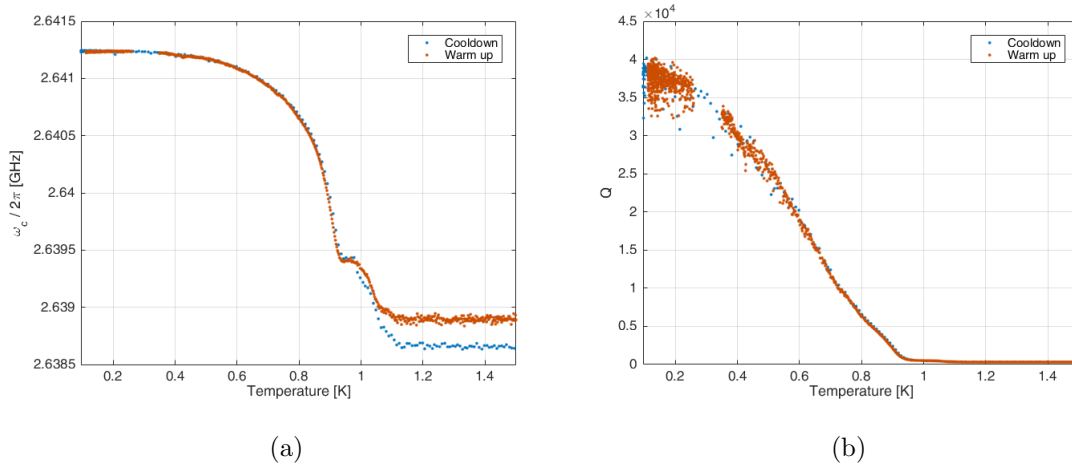
Figure 7.7: **Comparison of ω_c and Q of the improved cavity** during cooldown and warm up. (a) Due to the down-scaled cavity body, the temperature dependence of ω_c does not deviate for cooldown and warm up. (b) Also Q does not deviate for cooldown and warm up. The unstable Q indicates distortions of the cavity.

The measurements of the empty cavity with improved design were affected by distortions of unknown origin. These distortions showed up early summer 2016 and never vanished since then. It seems that an other experiment at the facility creates strong altering magnetic fields which penetrate our set-up. Time dependent magnetic fields influence superconductors and can yield quenching. Therefore, we observe irruptions of the cavity transmission which reduce the cavities Q. These reduction of Q is illustrated in Fig. 7.7b. We measured a maximum Q of 4×10^5 for the improved cavity, which is less than the half of the result for the undisturbed prototype cavity.

Note that these distortions also occurred in measurements with the prototype cavity and in measurements in a dilution refrigerator with a slightly different spectroscopic set-up. Hence, we can exclude a systematic origin of the distortions and have to consider an external source. In Fig. 7.8 further examples for the observed distortions are given.
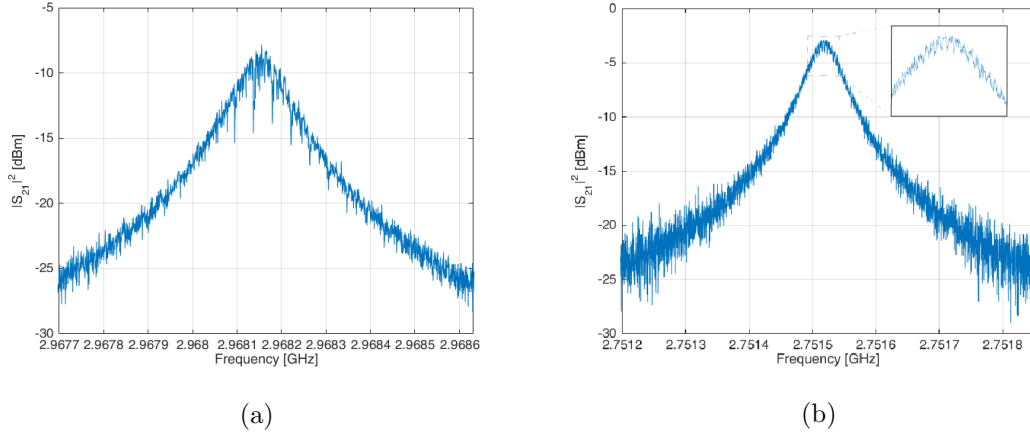
Figure 7.8: **Examples for traces with distortions.**(a) Trace taken while measuring the N1 sample. (b) Trace taken while measuring the E2 sample. Both traces were taken when the sample was completely relaxed at 100 mK.

However, the results of the spin-phonon relaxation measurements were not affected by these distortions because the cavities were still good enough to resolve the dispersive shift and the distortion creating field is far too weak to effect the NV^- level structure via Zeeman splitting. Only distortion induced jumps of ω_c would have affected the results. Though, we generated a sufficient set of data without such jumps of ω_c to generate valid results. Furthermore, we were able to reduce the distortion by shielding the cavity with a mu-metal cylinder with an inner lead cover.

7.4 Relaxation rate measurements

In order to evaluate the temperature dependent relaxation rate, we consider examples for measurements with both cavities. Since the eigenfrequency of the improved cavity is below the spin transition frequency, we observe a negative shift (see Fig. 7.9). On the other hand has the prototype cavity a higher eigenfrequency compared to the spin transition and, therefore, we observe a positive shift (see Fig. 7.10).
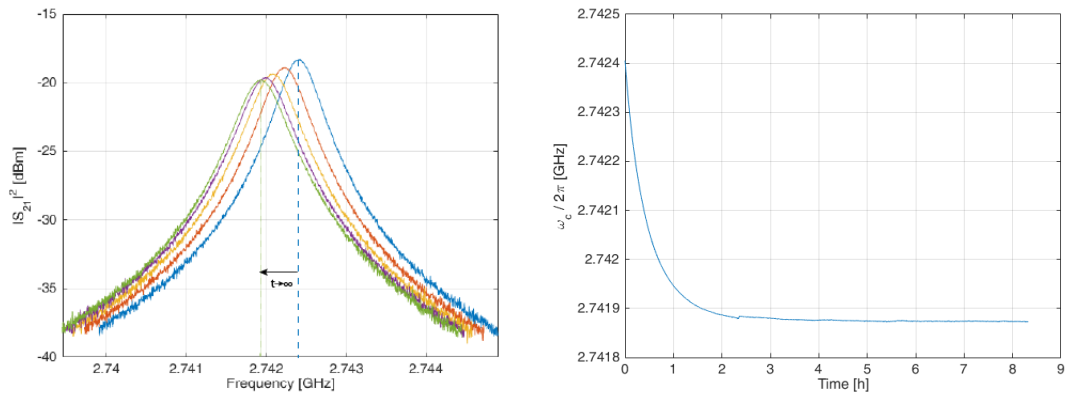
Figure 7.9: **Observed shift of N1 at** $80\,\mathrm{mK}$. The measurement was taken with the improved cavity.
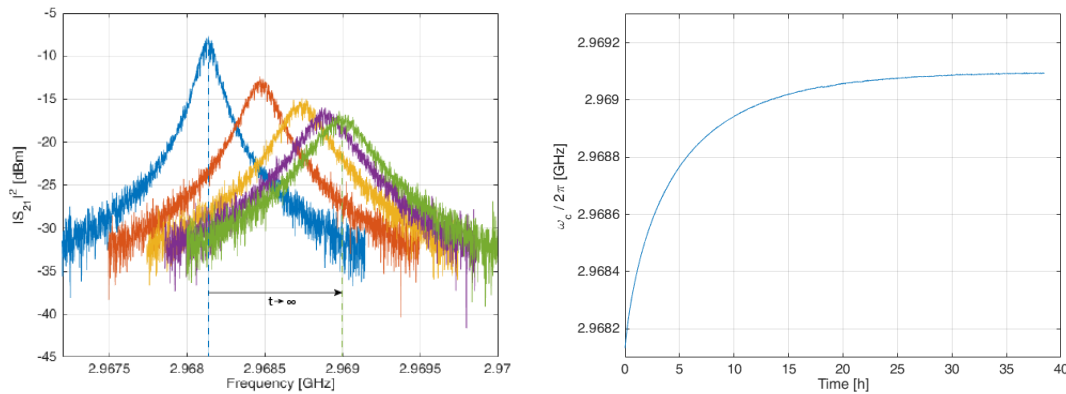
Figure 7.10: **Observed shift of E1 at** $80\,\mathrm{mK}$. The measurement was taken with the prototype cavity.

However, Eq. 7.2 describes an exponential decay of the spin polarization. Thus, $\Delta\chi$ grows inverse exponentially and the temperature dependent relaxation rate $\Gamma_1(T)$ can be determined with exponential fits:

$$\Delta\chi(T,t) = A \cdot \Big(1 - \exp\big(-\Gamma_1(T) \cdot t\big)\Big), \tag{7.5}$$

for positive shifts and

$$\Delta\chi(T,t) = \chi(T,t_0) - A \cdot \exp\big(-\Gamma_1(T) \cdot t\big), \tag{7.6}$$

for negative shifts.
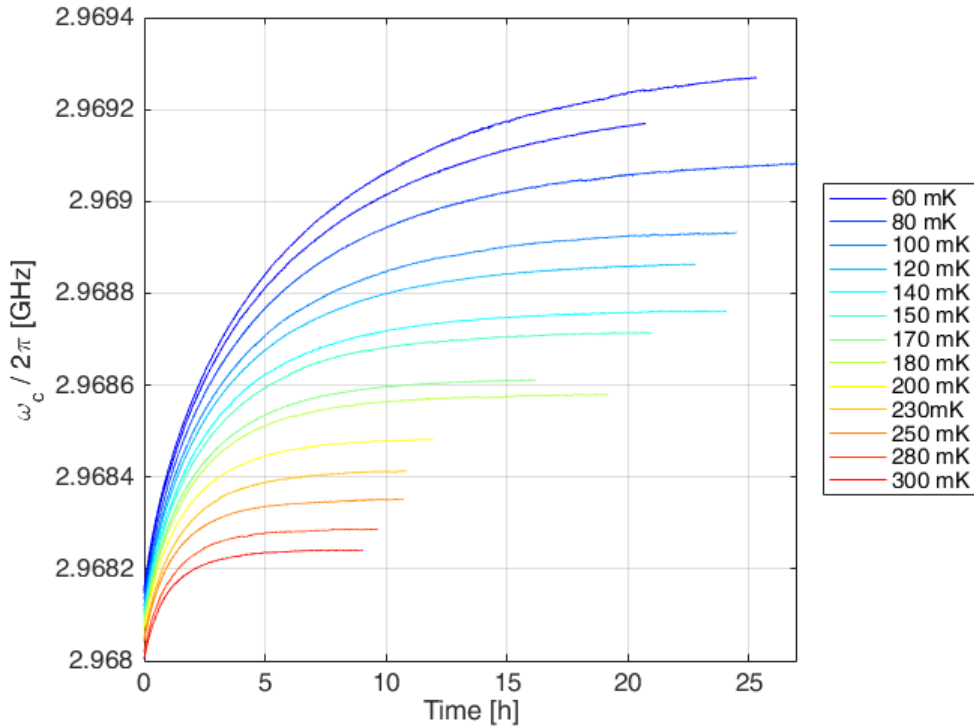
Figure 7.11: **Measurement of the temperature dependent cavity shift induced by the E1 sample.** The relaxation time increases for decreasing temperatures. At 60 mK the cooling energy of the ADR was not sufficient for the spin ensemble to relax completely in thermal equilibrium.

Next, we measure the spin-phonon relaxation for each sample stepwise in a temperature range from 60-300 mK to generate a set of temperature dependent relaxation rates

$\Gamma_1(T)$. In Fig. 7.11, the complete set of data of the E1 sample is shown. The results of the measurements of the other samples can be found in App. B. We observed remarkably long spin lifetimes of up to 8 h yielding to the conclusion that the spin-phonon coupling of NV^- in diamond is weak and that spin-phonon coupling of NV^- center is not a collective effect, but intrinsic to the single NV^-.

To show that Γ_1 is only dependent to the lattice temperature and, therefore, dependent to the phonon population, we measured inverse relaxations. Hence, the sample was stabilized at low temperatures until thermal equilibrium was reached. Afterwards, the temperature was increased and stabilized again. The occurring relaxation was measured. Fig. 7.12 gives an comparison of both relaxation measurement schemes at 200 mK and 300 mK. Besides that the cavity relaxes into the same thermal equilibrium state for both schemes, we were able to show that the measured relaxation rates correspond sufficiently. At 200 mK the measured relaxation time is $T_1 = 130 \pm 15$ min for both schemes and at 300 mK we measured $T_1 = 80 \pm 7$ min. Thus, we showed that spin-phonon relaxation is only dependent to the phonon population and that the here applied scheme of spin polarization measurement is correct.
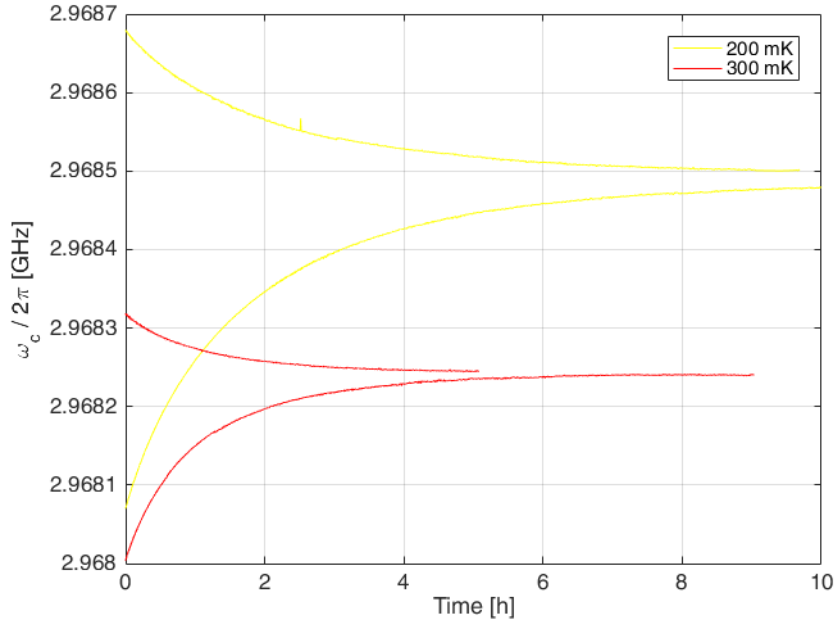
Figure 7.12: **Comparison of measured relaxation of positive and negative polarized spin polarization in reference to the thermal equilibrium.** The measured relaxation rate is only dependent to the phonon population.

7.4.1 Dilution refrigerator measurements

In order to determine the underlying spin-phonon relaxation process, it was necessary to measure the relaxation rate at temperatures below $50\,\mathrm{mK}$, where the thermal phonon population at the spin transition frequency is mostly suppressed. By reason of the limitation of the minimum base temperature of $50\,\mathrm{mK}$ in the ADR, we took additional data in a standard dilution refrigerator (Oxford DR-200). Since a dilution refrigerator has only a certain cooling power, we had to adapt the measurement sequence. For the initialization of the spin ensemble at $1\,\mathrm{K}$ and temperature control, we used an integrated electric heater. This measurement scheme enabled to take data at minimum base temperature of $\approx 25\,\mathrm{mK}$.

In Fig. 7.13, three measurements of the E1 sample taken in the dilution refrigerator are shown. The measurement showed the expected exponential behaviour, but was strongly affected by distortions and it is reasonable to consider a higher system-
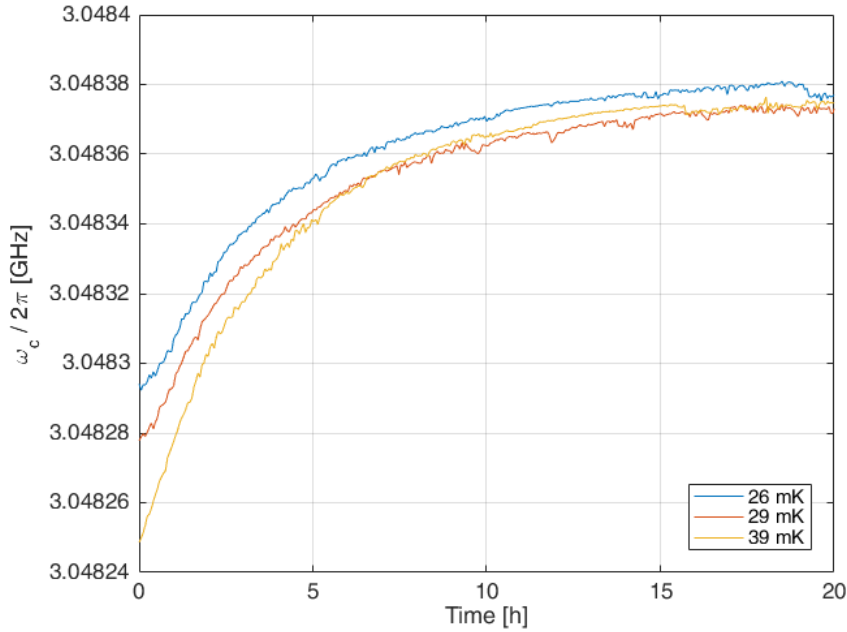
Figure 7.13: **Measurements of the E1 sample in the dilution refrigerator.** Compared to the measurements taken in the ADR (Fig. 7.11) the data taken in the dilution refrigerator are stronger affected by distortions.

atic error compared to the measurements taken in the ADR. However, the taken data match expected results and at higher temperatures, in the dilution refrigerator measured relaxation rates correspond to the results of the ADR measurements.

7.4.2 Calculation of the collective coupling strength

Next, we want to determine the enhanced collective coupling strength. Therefore, we calculate the difference of the dispersive shift for two steady states at temperatures T_1 and T_2, given by

$$\Delta\chi\left(T_2, T_1\right) = \chi\left(T_2\right) - \chi\left(T_1\right) = \frac{3g_N^2}{\Delta}\left(\langle S_z^2\rangle(T_2) - \langle S_z^2\rangle(T_1)\right) \tag{7.7}$$

We can transform this equation to get an expression for the collective coupling strength g_N:

$$g_N = \sqrt{\frac{\Delta\chi \cdot \Delta}{3\,\Delta\langle S_z^2\rangle}} \tag{7.8}$$

59

For the determination of the detuning Δ, we measured the resonance frequency of the flooded cavity to get ω_c and the values of $\Delta\langle S_z^2\rangle$ were calculated with (Eq. 7.1) . In Table 7.2 the calculated coupling strengths for the diamond samples are presented.

Sample	N1	E1	E2	E3
g_N[MHz]	6.62 ± 0.20	9.11 ± 0.58	5.88 ± 0.20	2.85 ± 0.19

Table 7.2: **Collective coupling strength.** The enhancement of coupling strength scales with the NV^- density and the sample size.

7.5   Determination of the Spin-Phonon Relaxation Process

In Sec. 5.5 we already introduced direct spin-phonon relaxation for the NV^- and found an expression for the temperature dependent relaxation rate, given as

$$\Gamma_1(T) = \Gamma_0\big(1 + 3\bar{p}_0(T)\big), \tag{7.9}$$

where

$$\bar{p}_0(T) = \frac{1}{e^{\frac{\hbar\omega_s}{k_B T}} - 1} \tag{7.10}$$

is the phonon population given by the Bose-Einstein distribution.

When we apply this model of direct spin-phonon relaxation on the taken data, we see that the model and data correspond well. We observe the predicted linear dependence for temperatures $T \geq 138.2\,\mathrm{mK}$. Furthermore, we observe a temperature independent relaxation rate Γ_0 at $T \leq 50\,\mathrm{mK}$. In this temperature regime, the thermal phonon occupation is mostly suppressed. Only spontaneous emission of spin excitations into the phononic vacuum can occur. The rate of spontaneous emission is only dependent to the sample specific phononic vacuum fluctuations at $\hbar\omega_s$.

As we can see in Fig. 7.14 and in Tab. 7.3, Γ_0 is strongly dependent to the lattice damage caused by the NV^- ensemble creation. For the neutron irradiated sample, Γ_0 is higher by one order of magnitude compared to the electron irradiated samples. Due to the higher rest mass of neutrons compared to electrons, neutron irradiation causes higher lattice damage and broadens the phonon band of the diamond lattice. If we compare $\Gamma_1(T)$ of sample E1 and E2 which were prepared identically, but have different NV^- densities (see Tab. 7.1), it appears that the relaxation rate is almost independent from

the NV^- density. Furthermore, when we take the sample E3 into account, we notice that for electron irradiated samples, the relaxation rate is also determined by the lattice damage, which is strongly dependent to the electron energy.
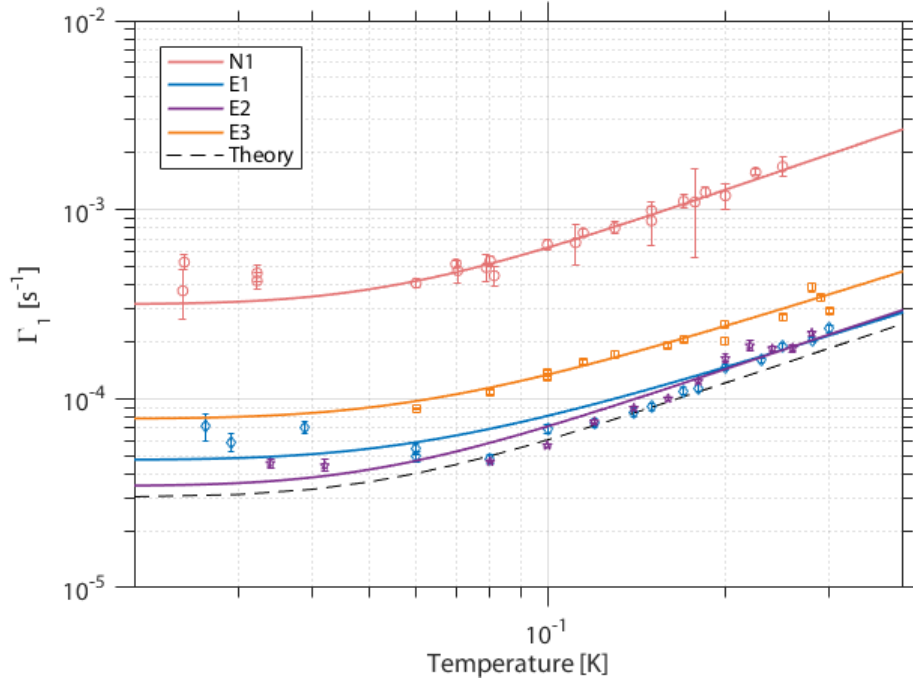

Figure 7.14: **Temperature dependence of the spin-phonon relaxation rate.** Data points in different color represent the measured data for different samples. Continuous lines indicate the fit of the relaxation rate corresponding to (Eq. 7.9). In the regime of $k_bT < \hbar\omega_s$ the relaxation rate is only dependent by spontaneous emission into the phononic vacuum modes. However, the rate for spontaneous emission Γ_0 is strongly dependent to the lattice damage caused by the NV^- ensemble creation method. The dashed line indicates *ab initio* calculations.

We want to conclude the discussion of the spin-phonon relaxation process with a comparison of the measurement results with theoretical calculations done by J.Gugler [63]. In order to generate an interaction Hamiltonian for the spin-phonon interaction, the Hamiltonian for dipolar spin-spin interaction was expanded for small ionic displacements. In the low temperature regime, phonons induce only small ionic displacements and, therefore, the Taylor expansion of the spin-spin interaction Hamiltonian is valid. For

Sample	N1	E1	E2	E3
$\Gamma_0[s^{-1}]$	$3.17(10) \times 10^{-4}$	$4.76(26) \times 10^{-5}$	$3.47(16) \times 10^{-5}$	$7.86(60) \times 10^{-5}$

Table 7.3: **Comparison of spontaneous emission rates** Γ_0. The measured rate of spontaneous emission is strongly dependent to the NV^- creation method.

the calculation of the temperature dependent relaxation rate, Fermi's golden rule for the $|m_s = 0\rangle \leftrightarrow |m_s = \pm 1\rangle$ transitions was applied only considering single spin-flip terms of the interaction Hamiltonian. For the calculations of the spin orbitals and phononic band, *ab initio* calculations using density functional theory was performed on a supercell containing 64 lattice sites with a single NV^-. The theoretical result for the relaxation rate is illustrated as dashed line in Fig. 7.14. It is remarkably that the theoretical model is consistent with the measured data of the electron irradiated samples. It appears that samples E1 and E2, which were irradiated with a large dose and annealed at high temperatures, almost show behaviour of a single NV^- in a perfect diamond lattice.

Chapter 8

Conclusion & Outlook

In this thesis, a new method for the measurement of solid-state electron spin-phonon relaxation in a low temperature regime was presented. The resonant mode of the newly designed 3D lumped element microwave resonator creates a homogeneous oscillating magnetic field which is used for coupling to the spins provided by a NV^- ensemble in diamond. Collective effects enhance the coupling strength and enable the measurement. The $\sqrt{N}$ scaling of the enhancement was shown, we measured $g_N = 2.85$ - $6.62\,\mathrm{MHz}$ compared to $g_0 = 38\,\mathrm{mHz}$ of the single spin.

In dispersive regime, where $\omega_s - \omega_c \gg g_N$, the cavity experiences a shift of the resonance frequency dependent to the polarization of the NV^- ensemble. Therefore, an indirect, non destructive measurement of the spin polarization is realized. Furthermore, this transmission spectroscopy does not utilize optical readout and enables to measure spin-phonon relaxation in a temperature regime of 25-300 mK for the first time.

The observed relaxation rates are strongly dependent on the phonon density at the spin-transition energy and, therefore, dependent on the NV^- generation method. Characteristic longitudinal relaxation times of up to $T_1 \approx 8\,\mathrm{h}$ were measured, which indicate weak spin-phonon coupling. A general estimation of the limit of the coherence time of the NV^- spin system is given.

The measurement of the relaxation rate at several temperatures in a range of 25-300 mK enabled the determination of the fundamental processes of spin-phonon interaction. We showed that at temperatures where $k_b T < \hbar\omega_s$, the population of phonons, mediating spin-phonon interaction becomes negligible and the longitudinal relaxation time is only limited by the spontaneous emission of spin excitations into the phononic

63

vacuum modes. At temperatures where $k_b T \geq \hbar \omega_s$, we observed the direct single phonon process with a linear temperature dependence of the relaxation rate. Furthermore, we compared our experimental results with theoretical calculations and found that samples, which were irradiated with a large dose of electrons and annealed at high temperatures almost show the calculated relaxation behaviour of a single NV^- in a perfect diamond crystal.

Next, we want to give an outlook for possible projects in the future. In [65], a proposal for a room-temperature diamond laser was presented. The presented system has a long longitudinal relaxation time T_1 and also superradiance was observed. Therefore, it matches the affordable properties to build a diamond maser at cryo-temperatures.

Furthermore, the generated understanding of spin-phonon interaction can be used to design materials with resonant phononic modes to provide spin ensemble cooling or heating. On the other hand, also materials with designed phononic band gaps are of interest and could be used for spin state insulation from environment or relaxation rate engineering.

Finally, the adaptation of the presented cavity design could also be used for the measurement of longitudinal relaxation of other solid-state spin systems like silicon-vacancy center in diamond. In general, application of the bow tie resonator with other quantum systems is possible and could be of interest.

Appendix A

Cavities used in experiment
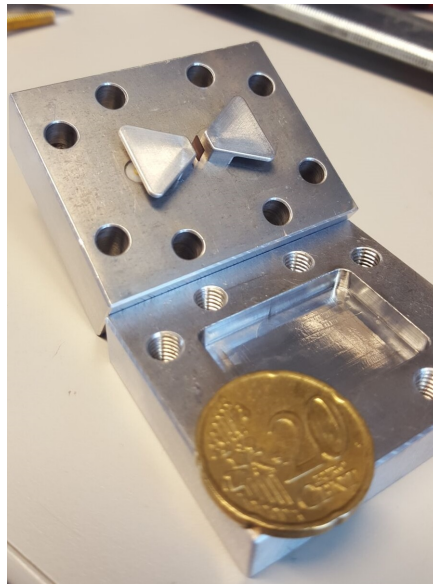
Figure A.1: **Picture of prototype cavity**. The E1 sample is attached to the cavity between the bow ties. Compared to the cavity with improved design, the prototype has a more massive body. The coin at the lid emphasizes the size of the cavity.
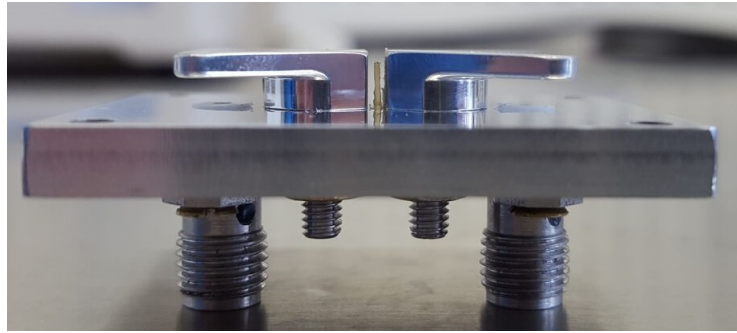
Figure A.2: **Picture of the cavity with improved design.** The E2 sample is attached to the cavity. The lid is removed.
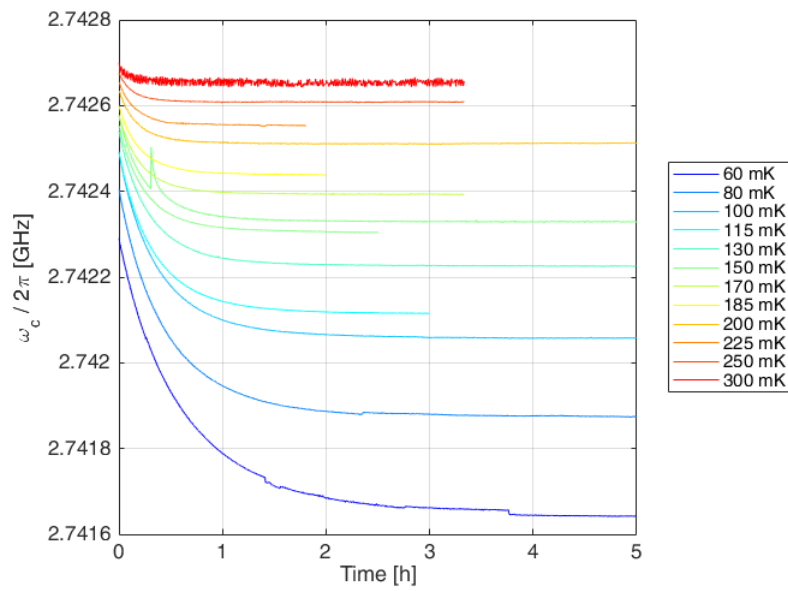
Appendix B

Relaxation measurements

Figure B.1: **Relaxation measurements of the N1 sample.**
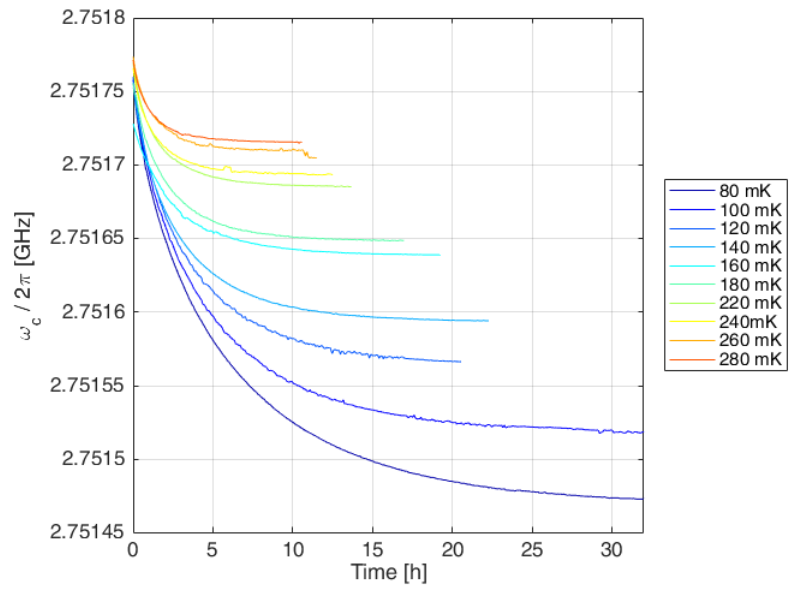
Figure B.2: **Relaxation measurements of the E2 sample.**
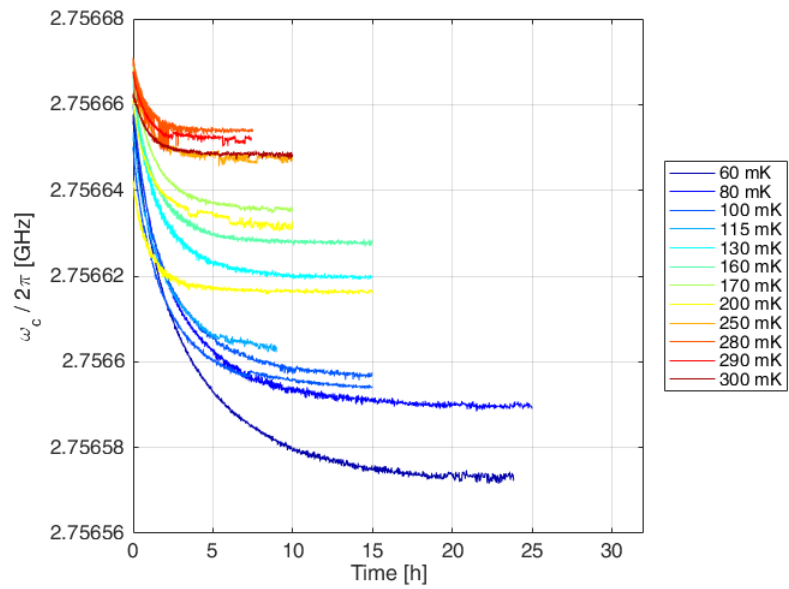
Figure B.3: **Relaxation measurements of the E3 sample.**

List of Figures

List of Tables

Bibliography

[1] Max Planck. Zur Theorie des Gesetzes der Energieverteilung im Normalspektrum. *Verhandlungen der Deutschen Physikalischen Gesselschaft*, 2:237, 1900.

[2] A. Einstein. Über einen die Erzeugung und Verwandlung des Lichtes betreffenden heuristischen Gesichtspunkt. *Annalen der Physik*, 322(6):132–148, 1905.

[3] E. Schrödinger. Quantisierung als Eigenwertproblem. *Annalen der Physik*, 384(6):489–527, 1926.

[4] W. Heisenberg. Über den anschaulichen Inhalt der quantentheoretischen Kinematik und Mechanik. *Zeitschrift für Physik*, 43(3-4):172–198, 1927.

[5] P. A. M. Dirac. The Quantum Theory of the Electron. *Proceedings of the Royal Society A: Mathematical, Physical and Engineering Sciences*, 117(778):610–624, 1928.

[6] Richard P. Feynman. Mathematical Formulation of the Quantum Theory of Electromagnetic Interaction. *Physical Review*, 80(3):440–457, 1950.

[7] T. H. MAIMAN. Stimulated Optical Radiation in Ruby. *Nature*, 187(4736):493–494, 1960.

[8] Hans Mooij. Superconducting quantum bits. *Physics World*, 17(12):29–33, 2004.

[9] Rainer Blatt and David Wineland. Entangled states of trapped atomic ions. *Nature*, 453(7198):1008–1015, 2008.

[10] Immanuel Bloch. Quantum coherence and entanglement with ultracold atoms in optical lattices. *Nature*, 453(7198):1016–1022, 2008.

[11] M. Saffman, T. G. Walker, and K. Mølmer. Quantum information with Rydberg atoms. *Reviews of Modern Physics*, 82(3):2313–2363, 2010.

[12] W. B. Gao, A. Imamoglu, H. Bernien, and R. Hanson. Coherent manipulation, measurement and entanglement of individual solid-state spins using optical fields. *Nature Photonics*, 9(6):363–373, 2015.

[13] Marcus W. Doherty, Neil B. Manson, Paul Delaney, Fedor Jelezko, J??rg Wrachtrup, and Lloyd C L Hollenberg. The nitrogen-vacancy colour centre in diamond. *Physics Reports*, 528(1):1–45, 2013.

[14] J. R. Maze, P. L. Stanwix, J. S. Hodges, S. Hong, J. M. Taylor, P. Cappellaro, L. Jiang, M. V. Gurudev Dutt, E. Togan, A. S. Zibrov, A. Yacoby, R. L. Walsworth, and M. D. Lukin. Nanoscale magnetic sensing with an individual electronic spin in diamond. *Nature*, 455(7213):644–647, 2008.

[15] Igor Aharonovich, Andrew D. Greentree, and Steven Prawer. Diamond photonics. *Nature Photonics*, 5(7):397–405, 2011.

[16] A. Jarmola, V. M. Acosta, K. Jensen, S. Chemerisov, and D. Budker. Temperature- and magnetic-field-dependent longitudinal spin relaxation in nitrogen-vacancy ensembles in diamond. *Physical Review Letters*, 108(19), 2012.

[17] A. Jarmola, A. Berzins, J. Smits, K. Smits, J. Prikulis, F. Gahbauer, R. Ferber, D. Erts, M. Auzinsh, and D. Budker. Longitudinal spin-relaxation in nitrogen-vacancy centers in electron irradiated diamond. *Applied Physics Letters*, 107(24), 2015.

[18] T. Astner, S. Nevlacsil, N. Peterschofsky, A. Angerer, S. Rotter, S. Putz, J. Schmiedmayer, and J. Majer. Coherent Coupling of Remote Spin Ensembles via a Cavity Bus. *Physical Review Letters*, 118(14), 2017.

[19] B. Hensen, H. Bernien, A. E. Dréau, A. Reiserer, N. Kalb, M. S. Blok, J. Ruitenberg, R. F. L. Vermeulen, R. N. Schouten, C. Abellán, W. Amaya, V. Pruneri, M. W. Mitchell, M. Markham, D. J. Twitchen, D. Elkouss, S. Wehner, T. H. Taminiau, and R. Hanson. Loophole-free Bell inequality violation using electron spins separated by 1.3 kilometres. *Nature*, 526(7575):682–686, 2015.

[20] F. Jelezko and J. Wrachtrup. Single defect centres in diamond: A review. *Physica Status Solidi (A) Applications and Materials Science*, 203(13):3207–3225, 2006.

[21] T Astner, J Gugler, A Angerer, S Wald, S Putz, N J Mauser, M Trupke, H Sumiya, S Onoda, J Isoya, J Schmiedmayer, P Mohn, and J Majer. Solid-state electron spin lifetime limited by phononic vacuum modes. *arXiv:1706.09798*, 2017.

[22] V. M. Acosta, E. Bauch, M. P. Ledbetter, A. Waxman, L. S. Bouchard, and D. Budker. Temperature dependence of the nitrogen-vacancy magnetic resonance in diamond. *Physical Review Letters*, 104(7), 2010.

[23] Y. Kubo, F. R. Ong, P. Bertet, D. Vion, V. Jacques, D. Zheng, A. Dréau, J. F. Roch, A. Auffeves, F. Jelezko, J. Wrachtrup, M. F. Barthe, P. Bergonzo, and D. Esteve. Strong coupling of a spin ensemble to a superconducting resonator. *Physical Review Letters*, 105(14), 2010.

[24] R. Amsüss, Ch Koller, T. Nöbauer, S. Putz, S. Rotter, K. Sandner, S. Schneider, M. Schramböck, G. Steinhauser, H. Ritsch, J. Schmiedmayer, and J. Majer. Cavity QED with magnetically coupled collective spin states. *Physical Review Letters*, 107(6), 2011.

[25] Andreas Angerer, Thomas Astner, Daniel Wirtitsch, Hitoshi Sumiya, Shinobu Onoda, Junichi Isoya, Stefan Putz, and Johannes Majer. Collective strong coupling with homogeneous Rabi frequencies using a 3D lumped element microwave resonator. *Applied Physics Letters*, 109(3), 2016.

[26] David M Pozar. *Microwave Engineering*. John Wiley & Sons, Inc., 4th edition, 2012.

[27] Daniel Wirtitsch. Simulation of the Bow Tie Resonator. Technical report, 2016.

[28] Brian C. Wadell. *Transmission line design handbook*. Artech House, 1991.

[29] D. F. Walls and Gerard J. . *Quantum Optics*. Springer, 2nd edition, 2008.

[30] Mark Fox. *Quantum Optics: An Introduction*, volume 67. Oxford University Press, 2006.

[31] Miguel Orszag. *Quantum optics: Including Noise Reduction, Trapped Ions, Quantum Trajectories, and Decoherence*. Springer, 3rd edition, 2016.

[32] F. W. Cummings and E.T. Jaynes. Comparison of Quantum and Semiclassical Radiation. *Ieee*, 51(1):89–109, 1963.

[33] David Zueco, Georg M. Reuther, Sigmund Kohler, and Peter Hänggi. Qubit-oscillator dynamics in the dispersive regime: Analytical theory beyond the rotating-wave approximation. *Physical Review A - Atomic, Molecular, and Optical Physics*, 80(3), 2009.

[34] Alexandre Blais, Ren Shou Huang, Andreas Wallraff, S. M. Girvin, and R. J. Schoelkopf. Cavity quantum electrodynamics for superconducting electrical circuits: An architecture for quantum computation. *Physical Review A - Atomic, Molecular, and Optical Physics*, 69(6), 2004.

[35] D I Schuster, a a Houck, J a Schreier, a Wallraff, J M Gambetta, A Blais, L Frunzio, J Majer, B Johnson, M H Devoret, S M Girvin, and R J Schoelkopf. Resolving photon number states in a superconducting circuit. *Nature*, 445(7127):515–518, 2007.

[36] R. H. Dicke. Coherence in spontaneous radiation processes. *Physical Review*, 93(1):99–110, 1954.

[37] Barry M Garraway. The Dicke model in quantum optics: Dicke model revisited. *Philosophical transactions. Series A, Mathematical, physical, and engineering sciences*, 369(1939):1137–1155, 2011.

[38] Michael Tavis and Frederick W. Cummings. Exact solution for an N-molecule-radiation-field Hamiltonian. *Physical Review*, 170(2):379–384, 1968.

[39] Michael Travis and Frederick W. Cummings. Approximate solutions for an N-molecule-radiation-field Hamiltonian. *Physical Review*, 188(2):692–695, 1969.

[40] K. Sandner, H. Ritsch, R. Amsüss, Ch Koller, T. Nöbauer, S. Putz, J. Schmiedmayer, and J. Majer. Strong magnetic coupling of an inhomogeneous nitrogen-vacancy ensemble to a cavity. *Physical Review A - Atomic, Molecular, and Optical Physics*, 85(5), 2012.

[41] M.H Levitt. *Spin Dynamics: Basics of Nuclear Magnetic Resonance*. John Wiley & Sons Ltd, 2nd edition, 2000.

[42] I. Waller. Über die Magnetisierung von paramagnetischen Kristallen in Wechselfeldern. *Zeitschrift für Physik*, 79(5-6):370–388, 1932.

[43] E. Heitler, W., Teller. Time Effects in the Magnetic Cooling Method. I. *Proceedings of the Royal Society A*, 155(886):629–639, 1936.

[44] R.de L. Kronig and C.J. Bouwkamp. Spin-levels and paramagnetic dispersion in iron-ammoniumalum. *Physica*, 6(3):290–298, 1939.

[45] J. H. Van Vleck. The Jahn-Teller Effect and Crystalline Stark Splitting for Clusters of the Form XY6. *The Journal of Chemical Physics*, 7(1):72–84, 1939.

[46] C.J. Gorter, P. Teunissen, and L.J. Dijkstra. On the apparent absence of paramagnetic disperson and absorption in titanium caesium alum. *Physica*, 5(10):1013–1017, dec 1938.

[47] R. J. Elliott. Theory of the effect of spin-Orbit coupling on magnetic resonance in some semiconductors. *Physical Review*, 96(2):266–279, 1954.

[48] R. Orbach. Spin-lattice relaxation in rare earth salts. *Proceedings of the Royal Society A*, 264(1319):458–484, 1961.

[49] P. L. Scott and C. D. Jeffries. Spin-lattice relaxation in some rare-earth salts at helium temperatures; observation of the phonon bottleneck. *Physical Review*, 127(1):32–51, 1962.

[50] P. Debye. Zur Theorie der spezifischen Wärme. *Annalen der Physik*, 344(14):789–839, 1912.

[51] K. N. Shrivastava. Theory of Spin–Lattice Relaxation. *Physica Status Solidi (B)*, 117(2):437–458, 1983.

[52] A M Stoneham. The phonon bottleneck in paramagnetic crystals. *Proceedings of the Physical Society*, 86(6):1163, 1965.

[53] Inc. High Precision Devices. Web Page. `http://www.hpd-online.com/103{_}cryostat.php`, (18.10.2017).

[54] W. E. Gifford and R. C. Longsworth. Pulse-Tube Refrigeration. *Transactions of the ASME Journal of Engeenering for Industry*, 86(3):264–268, 1964.

[55] Zhu Shaowei, Wu Peiyi, and Chen Zhongqi. Double inlet pulse tube refrigerators: an important improvement. *Cryogenics*, 30(6):514–520, 1990.

[56] Y. Matsubara and J. L. Gao. Novel configuration of three-stage pulse tube refrigerator for temperatures below 4 K. *Cryogenics*, 34(4):259–262, 1994.

[57] N. Jiang, U. Lindemann, F. Giebeler, and G. Thummes. A 3He pulse tube cooler operating down to 1.3 K. *Cryogenics*, 44(11):809–816, 2004.

[58] E. Warburg. Magnetische Untersuchungen. *Annalen der Physik*, 13:141, 1881.

[59] P. Debye. Einige Bemerkungen zur Magnetisierung bei tiefer Temperatur. *Annalen der Physik*, 386(25):1154–1160, 1926.

[60] W. F. Giauque. A thermodynamic treatment of certain magnetic effects. A proposed method of producing temperatures considerably below 1 absolute. *Journal of the American Chemical Society*, 49(8):1864–1870, 1927.

[61] Vitalij K. Pecharsky and Karl A. Gschneidner Jr. Magnetocaloric effect and magnetic refrigeration. *Journal of Magnetism and Magnetic Materials*, 200(1-3):44–56, 1999.

[62] Mariusz Mrózek, Daniel Rudnicki, Pauli Kehayias, Andrey Jarmola, Dmitry Budker, and Wojciech Gawlik. Longitudinal spin relaxation in nitrogen-vacancy ensembles in diamond. *EPJ Quantum Technology*, 2(1):22, 2015.

[63] J Gugler, T Astner, A Angerer, J Majer, J Schmiedmayer, and P Mohn. Ab initio calculation of the spin lattice relaxation time T1 for nitrogen-vacancy centers in diamond. *Manuscript in preparation*, 2017.

[64] Tobias Nöbauer, Kathrin Buczak, and Andreas Angerer. Creation of ensembles of nitrogen-vacancy centers in diamond by neutron and electron irradiation. *arXiv:1309.0453*, 2013.

[65] Liang Jin, Matthias Pfender, Nabeel Aslam, Philipp Neumann, Sen Yang, Jörg Wrachtrup, and Ren-Bao Liu. Proposal for a room-temperature diamond maser. *Nature Communications*, 6:8251, 2015.

Acknowledgement

When I decided to study Physics and moved to Vienna, I didn't know what I should expect and if I'm capable for it. But pretty soon, it became apparent that I made the right choice, that I chose a path to expand my intellectual and personal horizon.

Now, a few years later my thesis is finished and the end of the studies is close. It is time to reflect all these years and thank all those people, who made all this possible with their support and commitment.

One and a half year ago, I joined the atomchip group at the Atominstitut. It is a wonderful bunch of people and I appreciate every single day in the lab and every single minute in the coffee corner with them. I want to thank especially,

Jörg Schmiedmayer, the head of the group for giving me the opportunity to work in his field of study.

Hannes Majer, the head of our small NV^- group for his warm welcome and his willingness to answer all my questions and to help whenever I needed it.

Tom and Andreas, my supervisors for everything. Without you, I would not have been able to do this work. I'm still wondering that you never lost patience with me and my questions. Hope there will be a few drinks beside the coffee corner in the future!

Michael Trupke, who introduced me to the NV^- and the atomchip group during my bachelor thesis.

Beside these people from the group, I want to thank my family. Mom and Dad, without your backup, your unrestricted support all this would not have been possible. You with my little sis, even if you're not little anymore Magdalena, you're all just great and I'm happy to have you.

Finally, I want to thank my friends, who accompany and enrich my life for many years. To name you all per person would expand this scope, but you know who is meant.